Current Biology

Article

Adhesion-Dependent Wave Generation in Crawling Cells

Highlights

- Regular traveling waves of protrusion emerge in highly adherent fish keratocytes
- Overexpression of the actin anti-capping protein VASP abolishes waving protrusion
- Waving protrusion depends on negative feedback between adhesions and VASP
- Three mechanochemical feedbacks constitute a module for excitable actin dynamics

Authors

Erin L. Barnhart, Jun Allard, Sunny S. Lou, Julie A. Theriot, Alex Mogilner

Correspondence

theriot@stanford.edu (J.A.T.),
mogilner@cims.nyu.edu (A.M.)

In Brief

Barnhart et al. combine experimental manipulations with mathematical modeling to define the mechanochemical interactions underlying actin network excitability in highly adherent fish keratocytes. Traveling waves of protrusion emerge due to feedback among adhesions, the actin anti-capping protein VASP, membrane tension, and actin network growth.

Barnhart et al., 2017, Current Biology *27*, 27–38
January 9, 2017
http://dx.doi.org/10.1016/j.cub.2016.11.011

Current Biology
Article

Adhesion-Dependent Wave Generation in Crawling Cells

Erin L. Barnhart,[1,6] Jun Allard,[2,6] Sunny S. Lou,[1,3] Julie A. Theriot,[1,4,*] and Alex Mogilner[5,7,*]
[1]Department of Biochemistry and Howard Hughes Medical Institute, Stanford University School of Medicine, Stanford, CA 94305, USA
[2]Department of Mathematics and Department of Physics, University of California, Irvine, Irvine, CA 92697, USA
[3]Department of Chemical and Systems Biology, Stanford University, Stanford, CA 94305, USA
[4]Department of Microbiology and Immunology, Stanford University, Stanford, CA 94305, USA
[5]Courant Institute and Department of Biology, New York University, New York, NY 10012, USA
[6]Co-first author
[7]Lead Contact
*Correspondence: theriot@stanford.edu (J.A.T.), mogilner@cims.nyu.edu (A.M.)
http://dx.doi.org/10.1016/j.cub.2016.11.011

SUMMARY

Dynamic actin networks are excitable. In migrating cells, feedback loops can amplify stochastic fluctuations in actin dynamics, often resulting in traveling waves of protrusion. The precise contributions of various molecular and mechanical interactions to wave generation have been difficult to disentangle, in part due to complex cellular morphodynamics. Here we used a relatively simple cell type—the fish epithelial keratocyte—to define a set of mechanochemical feedback loops underlying actin network excitability and wave generation. Although keratocytes are normally characterized by the persistent protrusion of a broad leading edge, increasing cell-substrate adhesion strength results in waving protrusion of a short leading edge. We show that protrusion waves are due to fluctuations in actin polymerization rates and that overexpression of VASP, an actin anti-capping protein that promotes actin polymerization, switches highly adherent keratocytes from waving to persistent protrusion. Moreover, VASP localizes both to adhesion complexes and to the leading edge. Based on these results, we developed a mathematical model for protrusion waves in which local depletion of VASP from the leading edge by adhesions—along with lateral propagation of protrusion due to the branched architecture of the actin network and negative mechanical feedback from the cell membrane—results in regular protrusion waves. Consistent with our model simulations, we show that VASP localization at the leading edge oscillates, with VASP leading-edge enrichment greatest just prior to protrusion initiation. We propose that the mechanochemical feedbacks underlying wave generation in keratocytes may constitute a general module for establishing excitable actin dynamics in other cellular contexts.

INTRODUCTION

Many types of protrusion of the leading edge of motile cells are driven by actin polymerization [1]. In many cells, however, actin polymerization is offset by retrograde movement of the actin network, resulting in slow and unsteady protrusion in both time and space, with the leading edge advancing in pulses and protruding regions alternating with stalled regions [2–4]. One striking example of unsteady protrusion is traveling waves at the leading edge. These traveling waves have been observed in diverse cell types [3, 5–12] and represent a regular and relatively simple kind of unsteady protrusion event. Thus, elucidating the molecular and mechanical mechanisms that govern traveling-wave generation may illuminate general mechanisms that regulate leading-edge protrusion.

Traveling waves depend on three events: wave triggering, lateral propagation, and termination [13]. Two general classes of mechanisms—biochemical and mechanical—can contribute to each of these events. In purely biochemical models, amplification of stochastic fluctuations in actin polymerization activator concentrations triggers protrusion, diffusion of the activator allows for lateral propagation, and depletion of the activator or accumulation of an inhibitor terminates protrusion behind the wave front [6, 14–16]. Mechanical mechanisms can contribute to waving as well: slow incorporation of myosin molecules has been shown to drive actin network retrograde flow in a periodic fashion, terminating protrusion [4, 11], and theoretical work suggests that mechanical feedback between actin filaments and the cell membrane may drive lateral propagation of protrusion waves [17, 18]. In addition to these biochemical and mechanical mechanisms, the architecture of the lamellipodial actin network may also contribute to traveling-wave propagation, with actin barbed ends flowing laterally along the leading edge due to the branched architecture of the actin network near the leading edge [19].

Recently, several molecular pathways have been implicated in protrusion waves, including reaction-diffusion systems based on various activators and inhibitors, such as Scar/WAVE [6], Rac and Rho GTPases [7, 9, 14, 21], the Arp2/3 [20] complex [10], and phosphatidylinositol (3,4,5)-trisphosphate (PIP3) [20]. Furthermore, quantitative models for actin waves have evolved from useful conceptual models [15, 17–20] to models for protrusion waves based on and integrated with experimental data

[6, 10, 21, 22]. The main difficulty in quantitative understanding of the leading-edge waves is that, in most cell types, multiple mechanical, signaling, and actin turnover phenomena contribute to wave propagation and are hard to disentangle, especially when coupled to complex cell morphodynamics. In this paper, we overcome this difficulty by using fish epithelial keratocytes, cells with a less complex lamellipodial leading edge, streamlined for rapid locomotion that is largely uncoupled from actin flows [23] and signaling [24].

Although keratocytes normally exhibit steady global protrusions of a fan-shaped lamellipodial leading edge, when plated on highly adhesive substrates, they instead exhibit waves of protrusions [8]. Here, we show that the actin anti-capping protein VASP localizes to both the leading-edge and adhesion complexes in waving cells and that VASP overexpression switches highly adherent cells from waving protrusion of a short leading edge to persistent protrusion of a broad leading edge. This suggests that adhesion maturation near the leading edge depletes VASP, limiting the length of the leading edge and promoting waving. Based on this, as well as previously published models demonstrating that certain combinations of positive and negative feedbacks can trigger actin waves [19, 25, 26], we developed a mathematical model in which three feedback loops result in wave generation: positive rapid positive feedback between actin density and protrusion, negative local feedback between VASP and adhesions at the leading edge, and negative global feedback between membrane tension and protrusion. Simulations of this model recapitulated our experimental results, including the striking finding that qualitatively different modes of protrusion—persistent protrusion versus traveling waves—can emerge from quantitative change parameters such as cell-substrate adhesion strength and VASP density.

RESULTS

Highly Adherent Keratocytes Exhibit Traveling Waves of Protrusion

Fish epithelial keratocytes exhibit three types of leading-edge dynamics [8, 27]: (1) smooth protrusion of the entire leading edge; (2) noisy, or rough, protrusion; and (3) strikingly regular traveling waves of protrusion (Figure 1). Traveling waves of protrusion are associated with large-amplitude periodic oscillations in leading-edge velocity (Figures 1B and 1C) and a significant reduction in the fraction of the leading edge that protrudes at any given time (Figure 1D) compared to smooth or noisy cells (Figures 1H and 1L). Waves typically initiate at one side of the leading edge and then propagate along the entire length of the leading edge before extinguishing at the other edge; the next wave then initiates at the site of the original protrusion (Figure 1B; Figure S1). Wave initiation occasionally occurs at the center of the leading edge, in which case two waves propagate away from the site of initiation before terminating at either side of the leading edge (Figures S1B, S1F, and S1G). Noisy cells are characterized by irregular, highly variable leading-edge velocities (Figures 1F and 1G), whereas smooth cells exhibit very low leading-edge velocity variance (Figures 1J and 1K). Smooth cells occasionally exhibit synchronous oscillations of the entire leading edge but with substantially smaller amplitudes, shorter oscillation periods, and no lateral propagation (Figures S2A–S2C). We occasionally observed these low-amplitude, high-frequency oscillations on top of traveling waves (Figures S2D–S2F), suggesting that they may be driven by a different mechanism than traveling waves. The remainder of this work will focus primarily on potential mechanisms for traveling-wave formation and propagation.

We have previously shown that traveling waves emerge in highly adherent keratocytes [8]. To further examine the effects of cell-substrate adhesion strength on protrusion waves, we first plated keratocytes on glass surfaces functionalized with either intermediate or high concentrations of Arg-Gly-Asp (RGD) peptides (see Experimental Procedures for specific concentrations), as RGD is the integrin-binding motif found in extracellular matrix proteins such as collagen or fibronection [28], and we classified leading-edge dynamics in randomly selected populations of cells as smooth, noisy, or waving based on protrusion fraction and leading-edge velocity variance. As expected, traveling waves were more prevalent in keratocytes plated on high-RGD densities than in keratocytes plated on intermediate-RGD densities (Figure 1M). Next, we compared traveling waves in keratocytes plated on intermediate- and high-RGD densities by measuring several parameters (Figures 1N–1R, Figure S3): the period of leading-edge oscillations (wave period), the fraction of the leading edge that protrudes at any given time (protrusion fraction), the fraction of the wave period during which the leading edge is protruding (duty ratio), the maximum instantaneous boundary protrusion rate (protrusion speed), and the rate of lateral wave propagation (propagation speed). The strength of adhesion had no effect on the rate of boundary protrusion or lateral propagation (Figures 1Q and 1R). The wave period was reduced, and the duty ratio and protrusion fraction were both significantly increased in cells plated on intermediate RGD densities (average wave period = 189 s, duty ratio = 0.83, and protrusion fraction = 0.39; n = 3 cells), compared to cells plated on high-RGD densities (average wave period = 283 s, duty ratio = 0.47, and protrusion fraction = 0.3; n = 26 cells; Figures 1N–1P). Moreover, as previously described [8], these waves emerge in cells crawling on micropatterned surfaces immediately after the cell crossing from regions of intermediate adhesion to regions of high adhesion (Figure S4), indicating that traveling waves are dependent on local cell-substrate adhesion strength rather than long-term adaptation to different surfaces. Altogether, these results indicate that increasing cell-substrate adhesion strength promotes the formation of traveling waves and that the width and lifetime of the leading edge decrease with increasing adhesion strength.

Large Adhesions Near the Leading Edge Promote Waving

Highly adherent, waving keratocytes have large adhesions that localize near the leading edge, whereas smooth keratocytes have large adhesions only at the trailing edge (Figures 2A and 2B). Based on this—and on our results demonstrating that, as cell-substrate adhesion strength increases, waves emerge and the length of the leading edge decreases—we hypothesized that mature adhesions near the leading edge induce waving by locally inhibiting protrusion. If this is the case, then pharmacological perturbations that affect adhesion maturation and turnover in keratocytes plated on high-RGD densities should have

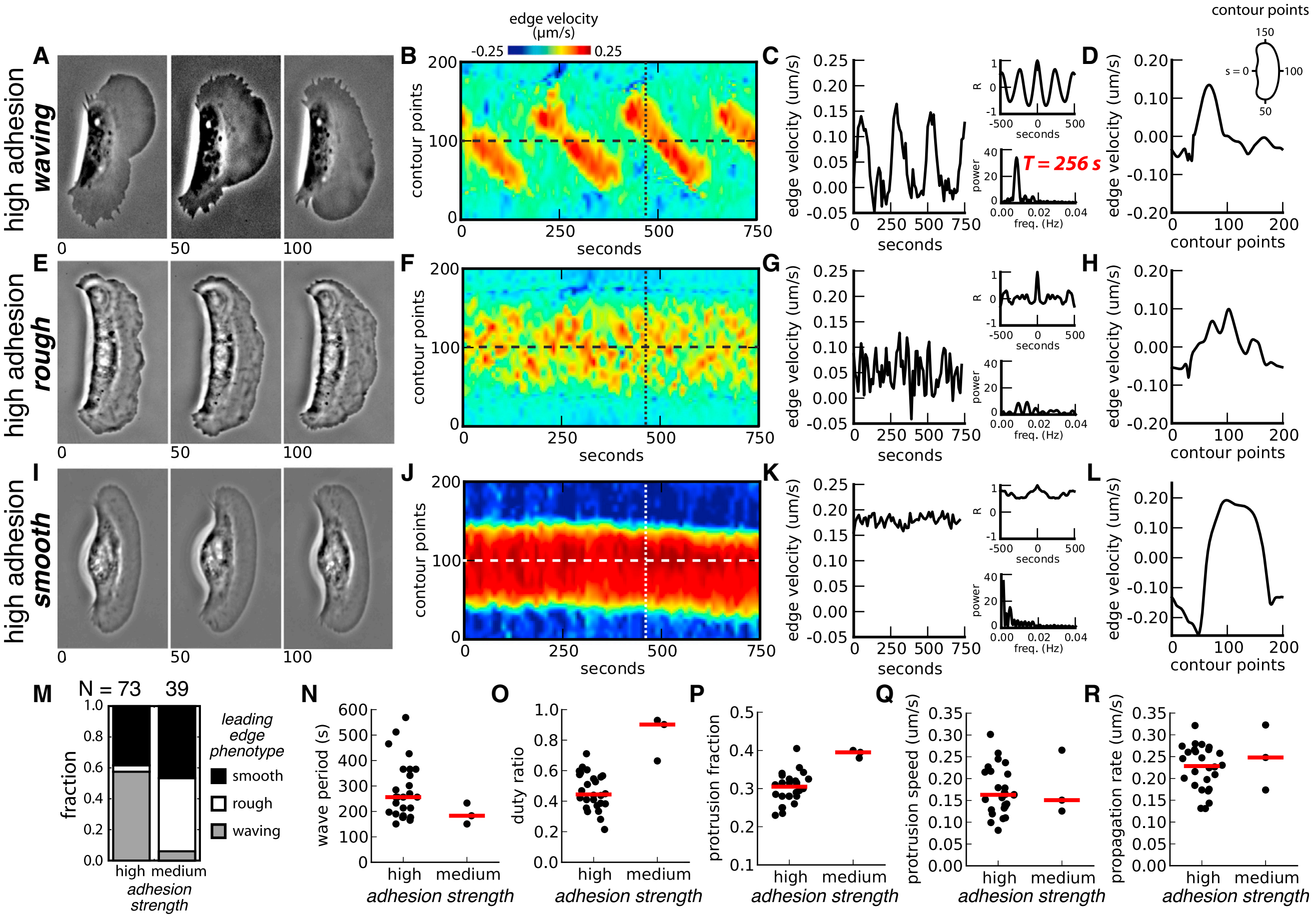

Figure 1. Leading-Edge Dynamics in Highly Adherent Keratocytes

(A–L) Phase images (A, E, and I); edge velocity maps (B, F, and J); velocity of the center of the leading edge, plotted over time (C, G, and K); and velocity along the leading edge, plotted versus cell boundary position (D, H, and L) for representative waving (A–D), rough (E–H), and smooth (I–L) cells, all plated on highly adhesive surfaces. The edge velocity maps show the speed of the cell boundary at each point around the cell perimeter, plotted over time. Hot colors represent protrusion of the cell boundary, and cold colors represent retraction. The insets in (C), (G), and (K) show the autocorrelation function for the edge velocity (top) and the power spectrum of the autocorrelation function (bottom). The period of oscillation of the leading edge for the waving cell is indicated on the power spectrum plot in red.

(M) The fraction of waving (gray), noisy (white), and smooth (black) cells in populations of cells plated on the indicated surfaces.

(N–R) Wave periods (N), duty ratios (O), protrusion fractions (P), protrusion rates (Q), and lateral propagation rates (R) for waving cells plated on surface coated with either high (n = 26 cells) or intermediate (n = 3 cells) RGD densities. The red lines indicate the median. Values from only three medium adhesion cells are reported, because a tiny fraction of medium-adhesion cells exhibit traveling waves.

See also Figures S1–S4.

predictable effects on waving. Specifically, perturbations that promote adhesion maturation or inhibit adhesion turnover should increase the fraction of the cells in a population that exhibit traveling waves, and these waving cells should have longer wave periods and smaller protrusion fractions and duty ratios. Perturbations that inhibit adhesion maturation should have the opposite effect. To test this, we first treated keratocytes with the focal adhesion kinase (FAK) inhibitor PF-573228 [29]. FAK inhibition has been shown to prevent focal adhesion turnover in several cell types [29]; consistent with this, larger adhesions localized to the leading edge in keratocytes treated with PF-573228, compared to control cells (Figure 2C). FAK inhibition increased the fraction of waving cells (Figure 2G), as well as increasing the wave period (Figures 2D–2F and 2H) and decreasing the boundary protrusion fraction and duty ratio (Figures 2I and 2J), consistent with our hypothesis. Adhesion maturation is also known to depend on myosin contraction [30]. The myosin inhibitor blebbistatin reduced the size of adhesions at the leading edge in keratocytes plated on high-RGD densities (Figure S5A) and reduced the fraction of waving cells (Figures S5B–S5E). Altogether, these results suggest that protrusion waves in highly adherent keratocytes depend on adhesion maturation near the leading edge.

Oscillations in Actin Polymerization Drive Protrusion Waves

Generation of the traveling waves we have observed in highly adherent keratocytes must depend on three steps: protrusion initiation, lateral propagation of protrusion along the leading edge, and local protrusion termination behind the wave front.

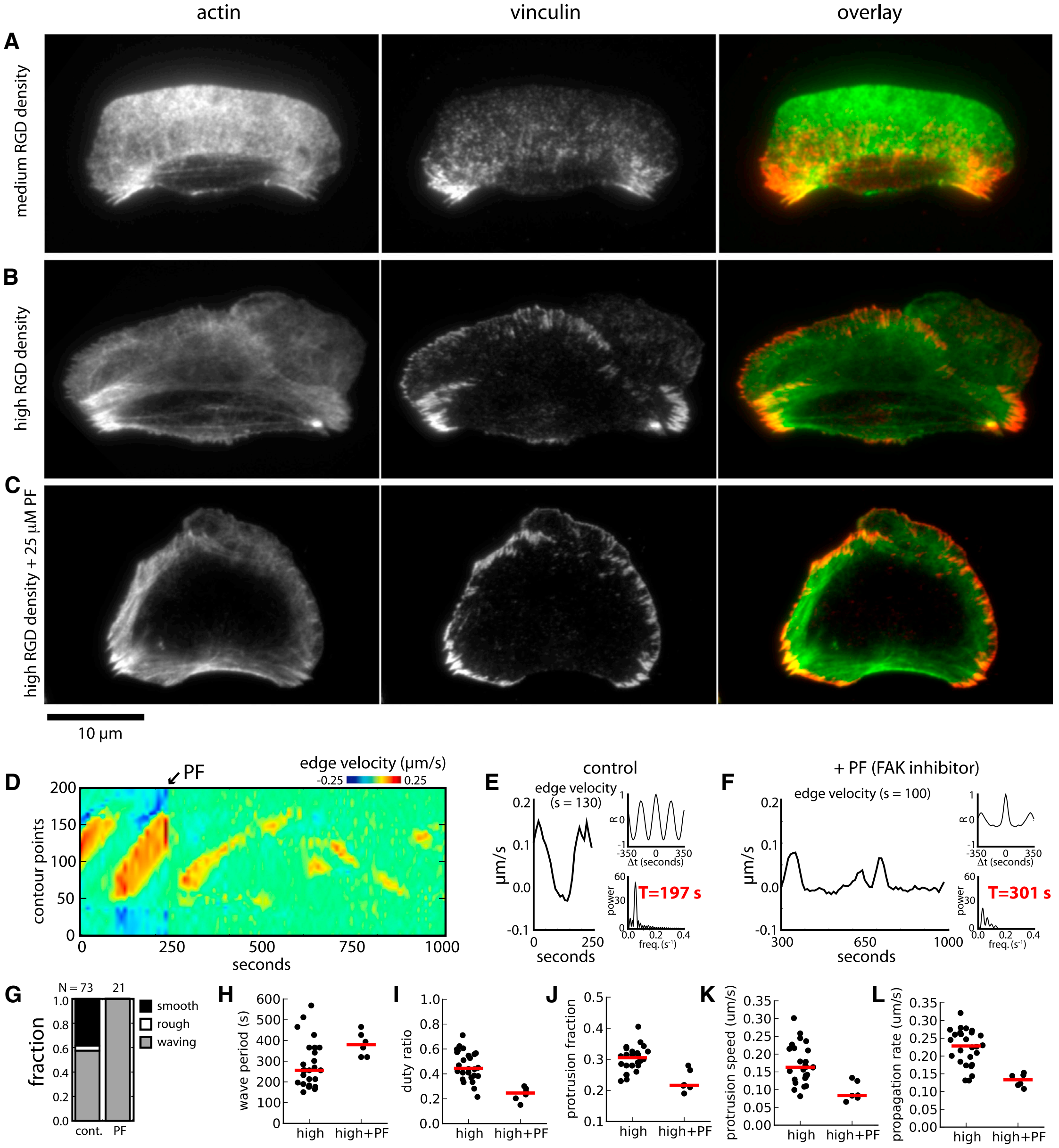

Figure 2. FAK Inhibition Prevents Adhesion Turnover and Increases Waving

(A–C) Images of cells plated on either intermediate (A) or high-adhesion-strength surfaces (B and C) and labeled for actin with fluorescent phalloidin and immunolabled for vinculin. The cells in (A) and (B) are control cells; the cell in (C) was treated with 25 µM of the FAK inhibitor PF-573228 (PF).

(D–F) Edge velocity map (D) and velocity of the center of the leading edge for a waving cell before (E) and after (F) treatment with PF. The upper insets in (E) and (F) are the autocorrelation functions for the edge velocity, and the lower insets are the power spectrums of the autocorrelation functions. The wave period increased from 197 s to 301 s after the addition of PF.

(G) The fraction of waving, rough, and smooth cells in populations of cells plated on high-adhesion-strength surfaces and treated with PF.

(H–L) Wave periods (H), duty ratios (I), protrusion fractions (J), protrusion rates (K), and lateral propagation rates (L) for control (n = 26 cells) or PF-treated waving cells (n = 5 cells). The red lines indicate the median. The control measurements shown in Figures 1M–1R are shown again here in (G)–(L) for ease of comparison. See also Figure S5.

Relative rates of actin polymerization and actin retrograde flow control protrusion: the cell membrane protrudes when actin polymerization rates exceed retrograde flow rates, and the membrane stalls or retracts when retrograde flow rates are equal to or greater than polymerization rates. Thus, adhesions near the leading edge could control wave initiation and termination by regulating actin polymerization or retrograde flow or both. To determine whether protrusion waves in highly adherent keratocytes are associated with oscillations in actin polymerization and/or retrograde flow, we measured actin network movement at stalled and protruding regions of the leading edge of waving cells using fluorescence speckle microscopy. We measured

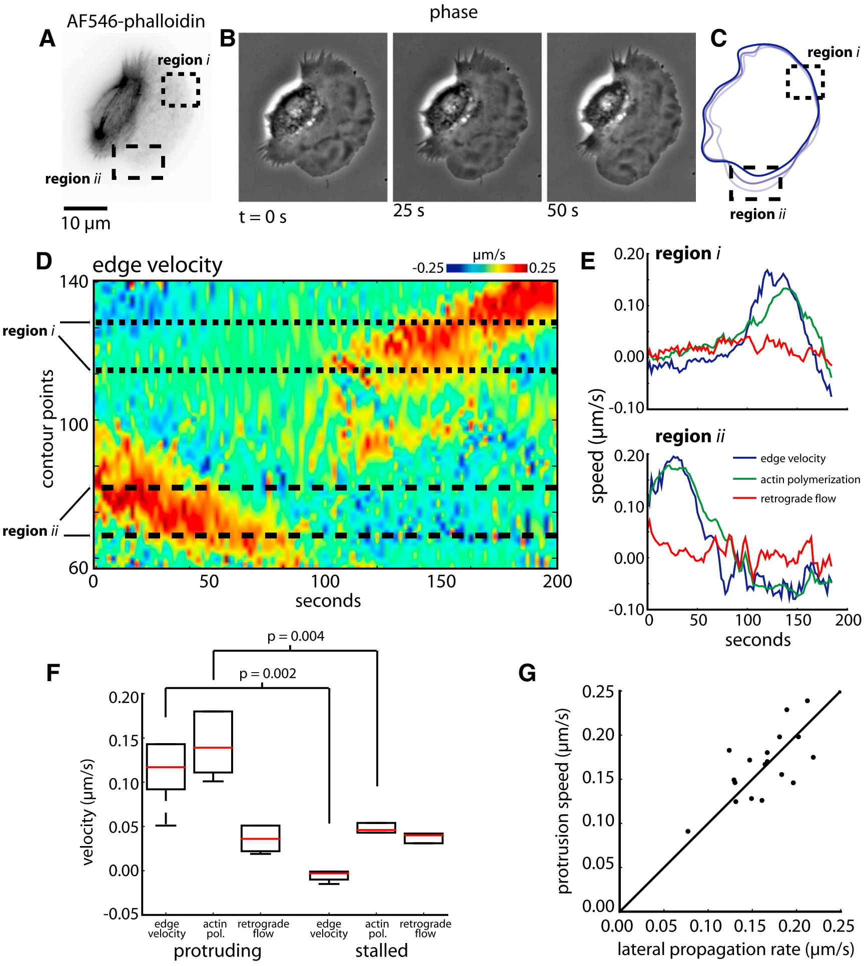

Figure 3. Cell Edge Velocities in Waving Cells Correlate with Actin Polymerization Rates, Not Retrograde Flow Rates

(A–C) Fluorescence image (A), phase images (B), and cell outlines (C) of a cell electroporated with fluorescent phalloidin and plated on a high-adhesion-strength surface.

(D and E) Edge velocity map (D) and edge velocity, actin polymerization, and actin retrograde flow plotted over time (E).

(F) Box-and-whisker plots showing cell-edge velocity, actin polymerization rates, and actin retrograde flow rates for stalled and protruding portions of the leading edge.

(G) The rate of protrusion of the leading edge plotted versus the rate of lateral wave propagation.

actin polymerization rates by measuring actin movement relative to the cell boundary, and we measured retrograde flow rates by measuring actin movement relative to the underlying substrate (Figure 3; see Experimental Procedures). First, we found that, although retrograde flow rates in protruding and stalled regions of the leading edge are equivalent (0.03 μm/s in both regions), actin polymerization was much faster in protruding regions (0.13 μm/s) than in stalled regions (0.03 μm/s; Figure 3F). Moreover, the rate of retrograde flow at a particular point along the leading edge remained constant over time, whereas the rate of actin polymerization correlated with the velocity of the cell edge (Figures 3D and 3E). Thus, oscillations in actin polymerization, rather than retrograde flow, drive wave initiation and termination: protrusion initiates when the polymerization rate exceeds the basal retrograde flow rate and terminates when polymerization falls below the retrograde flow rate.

In addition to mechanisms for triggering and terminating protrusion, traveling protrusion waves require a mechanism for spatial coupling of adjacent sections of the leading edge. This spatial coupling could be achieved by the diffusion of an actin regulator molecule [6, 10], in which case, the rate of lateral propagation should be proportional to the square root of the regulator's diffusion constant [13]. Alternatively, spatial coupling could be achieved by polymerization of the actin network itself, since Arp2/3-mediated branching of the network occurs at ±35° relative the direction of overall actin network growth [19]. Polymerization of this branched network, therefore, results in lateral flow of barbed ends along the leading edge. In this scenario, lateral propagation rates should be proportional to the protrusion velocity. Consistent with this second scenario, the rate of lateral propagation in waving keratocytes correlates with the maximal rate of leading-edge protrusion (Figure 3G).

Overexpression of VASP Reduces Waving in Highly Adherent Cells

Increasing adhesion strength causes a reduction in the length of the leading edge (Figure 1O), suggesting that adhesions may promote waving by titrating a limiting factor that promotes protrusion away from the leading edge. Adhesions are complex structures, and more than 100 different types of proteins have been shown to associate with mature focal adhesions [31]. Among these are several actin-modifying proteins, including the anti-capping protein VASP and the actin nucleators Arp2/3 and formins. VASP has previously been shown to localize to both the leading edge and adhesions in the rear in smooth and noisy keratocytes [27], and VASP localization patterns have been shown to correlate with modes of edge dynamics in spreading fibroblasts [32]. Based on this, we suspected that adhesions near the leading edge in highly adherent keratocytes may induce waving by depleting VASP from the leading edge. To test this, we examined the effects of overexpression of VASP by transfecting keratocytes with GFP-VASP, and then we plated transfected cells on surfaces coated with high-RGD densities. We found, first, that VASP localization patterns in waving and smooth cells were consistent with our assumption that mature adhesions compete VASP away from the leading edge: whereas in smooth cells VASP localized primarily to the leading edge (Figures 4B, 4E, and 4F), in waving cells, VASP localized to large adhesions near the front of the cell, as well as to short, protruding sections of the leading edge (Figures 4A, 4C, and 4D). The fraction of the cell perimeter enriched for VASP was also significantly reduced

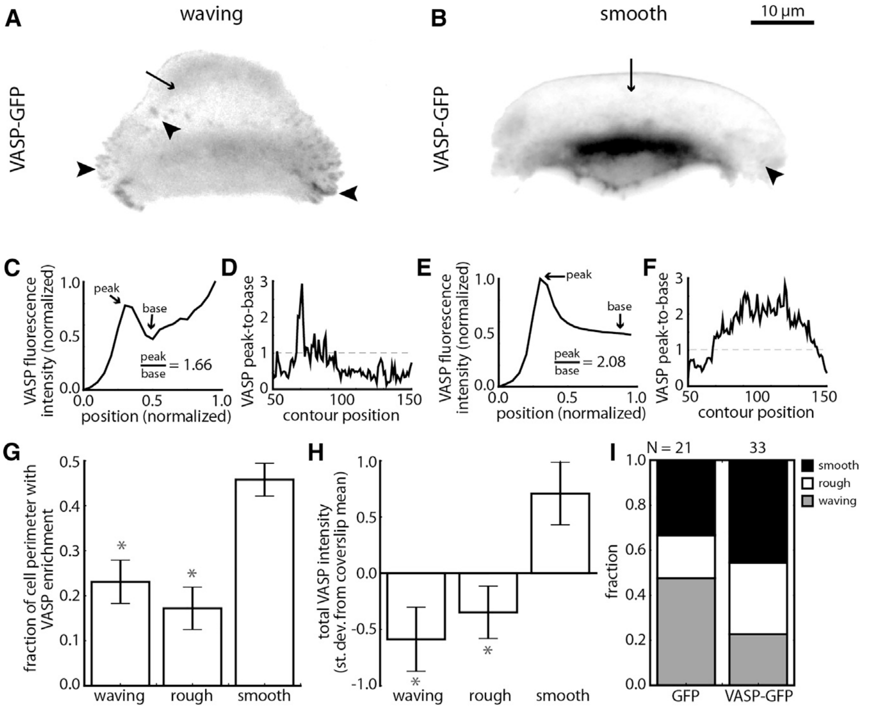

Figure 4. Overexpression of VASP-GFP Reduces Waving

Keratocytes were transfected with a VASP-GFP construct and plated on high-adhesion-strength surfaces.

(A and B) Images of waving (A) and smooth (B) cells expressing VASP-GFP. Arrows indicate enrichment of VASP-GFP at the leading edge and VASP localization to adhesions.

(C–F) The relative levels of VASP intensity at the leading edge for the waving cell in (A) (C and E) and the smooth cell in (B) (D and F). (C) and (E) show VASP intensity line scans indicated by the white arrows in (A) and (B). VASP peak-to-base ratios, calculated by dividing the highest fluorescence intensity at the cell edge (peak) by the lowest intensity interior to the cell boundary (base), are indicated on the graphs. (D) and (F) show peak-to-base ratios plotted versus position along the leading edge.

(G and H) Bar graphs showing the fraction of the cell perimeter with a peak-to-base ratio >1 (G) and the total VASP-GFP intensity (H) for waving, rough, and smooth cells; error bars indicate SEM, and red asterisks indicate significant differences from the smooth population (Student's t test, $p < 0.025$). Cell intensities were normalized to the mean intensity for each coverslip by subtracting the mean and dividing by the SD.

(I) The fraction of waving, rough, and smooth cells in populations expressing either VASP-GFP or GFP alone.

in waving cells compared to that in smooth cells (Figure 4G). Next, we found that the fraction of waving cells was reduced in cells expressing GFP-VASP, compared to that in cells expressing GFP alone (Figure 4I), and that within the population of GFP-VASP-expressing cells, smooth cells expressed higher levels of GFP-VASP than either waving or rough cells (Figure 4H). These results suggest that VASP is, indeed, a limiting factor required for actin polymerization and leading-edge protrusion in waving cells.

Mathematical Model for Adhesion- and VASP-Dependent Protrusion Waves

We propose a model in which adhesions near the leading edge promote traveling waves of protrusion by titrating VASP molecules away from the leading edge. Competition between the leading edge and adhesions for VASP promotes transient periods of high- and low-actin polymerization, and polymerization of the dendritically branched actin network transmits protrusion laterally along the leading edge. This model is based on four key experimental results. First, our measurements of actin polymerization and retrograde flow rates in waving keratocytes indicate that waving is the result of oscillations in actin polymerization rates rather than retrograde flow (Figure 3). Second, there is a tight correlation between the rates of leading-edge protrusion and lateral propagation of the protrusion wave (Figure 3G), suggesting that wave propagation is the result of actin polymerization itself rather than diffusion of an actin activator. Third, the fraction of cells that exhibit traveling waves—as well as the wave period, protrusion fraction, and duty ratio—depends on the localization of large adhesions near the leading edge (Figures 1 and 2; Figure S5). Finally, overexpression of VASP reduces the fraction of waving cells plated on highly adherent surfaces (Figure 4).

Based on these experimental observations, we developed a mathematical model in which traveling protrusion waves emerge from the dynamic interplay among mature adhesions, VASP, actin barbed ends, and membrane tension (Figure 5A); all model assumptions, equations, and parameters are described in detail in the Supplemental Experimental Procedures. In brief, in this model, we assume that protrusion occurs when the local density of actin barbed ends exceeds a critical threshold set by tension in the membrane [33]. The density of barbed ends depends on the local concentration of VASP, which increases barbed-end density by preventing capping [34]. We assume that VASP reaches the leading-edge barbed ends by diffusion, drift, or both [35], and VASP molecules that dissociate from barbed ends diffuse in the cytosol and may either re-associate with barbed ends or bind mature adhesions (Figure 5B). We assume that membrane protrusion involves three feedback loops (Figure 5A): (1) positive feedback with actin branching, in which branching rates increase as protrusion velocity increases [19]; (2) global negative feedback due to protrusion-dependent increases in membrane tension [36]; and (3) local negative feedback due to adhesion-dependent depletion of VASP from barbed ends at the leading edge. This local depletion is triggered by the protrusion-dependent formation of adhesions [37], which, we assume, bind VASP as they mature. Mature adhesions remain stationary with respect to the underlying surface [38, 39], and adhesion-bound VASP is, therefore, convected away from the leading edge by protrusion, locally depleting VASP from the leading edge. Finally, we assume that waves of protrusion propagate laterally along the leading edge, due to the branched architecture of the actin network, until

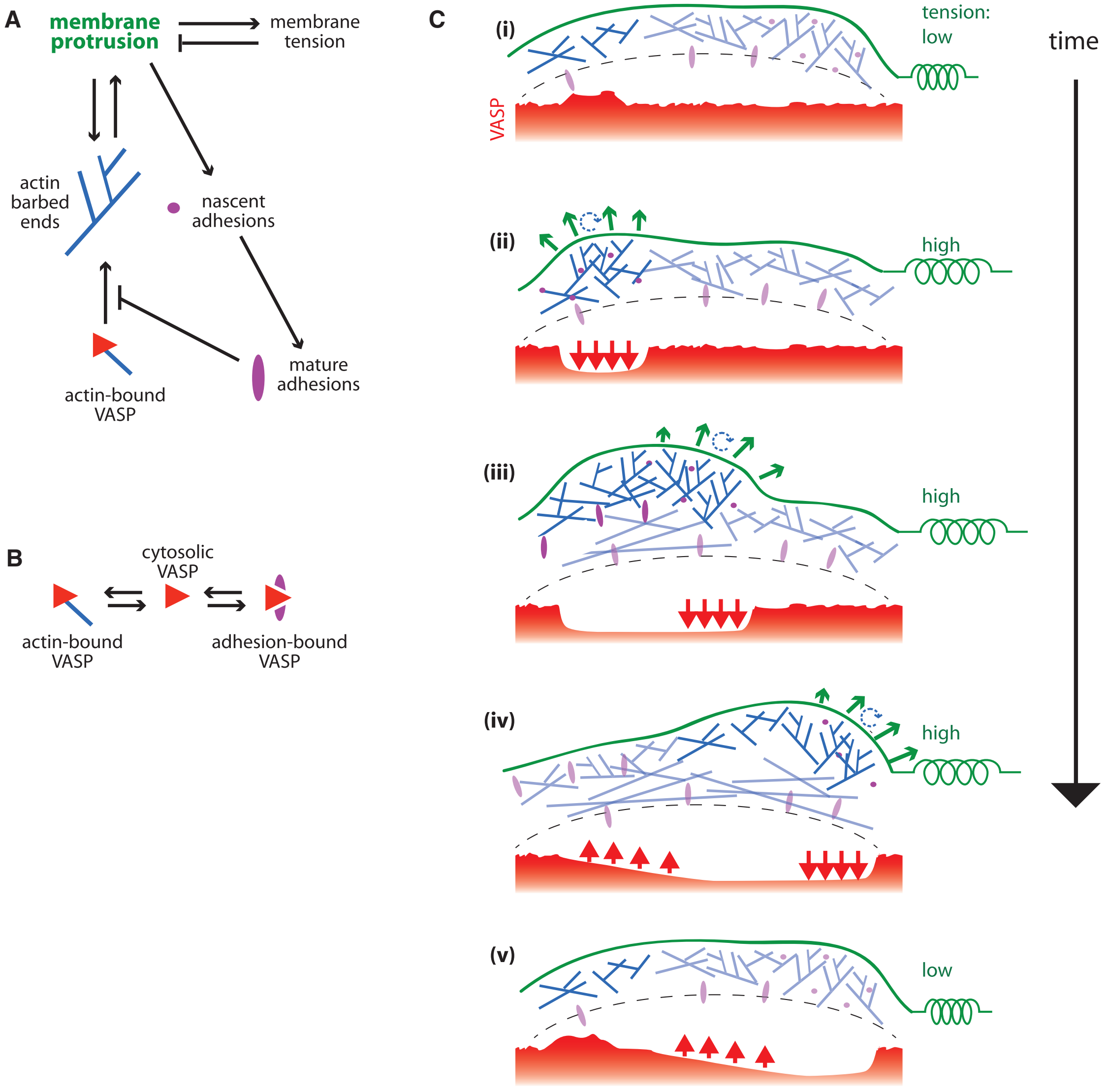

Figure 5. Model for Adhesion- and VASP-Dependent Traveling Wave Generation

(A) Diagram depicting feedbacks among membrane protrusion, membrane tension, adhesions, and actin barbed ends.

(B) VASP molecules bind adhesions or actin barbed ends, or they diffuse in the cytosol.

(C) Sequence of events during waving. At stalled portions of the leading edge in waving cells, the accumulation of VASP increases the density of barbed ends until protrusion begins, triggering positive feedback between protrusion and the branching rate (parts i and ii). This increase in protrusion also increases membrane tension, which serves to prevent the initiation of protrusion at any other point along the leading edge, limiting the cell to a single protrusion. The lateral flow of barbed ends (due to the branched architecture of the actin network) causes protrusion to spread along the leading edge (parts ii–iv). Protrusion induces adhesion formation, resulting in the depletion of VASP from the leading edge (indicated by the red arrows in parts ii–iv) and the eventual termination of protrusion behind the wave front. Waves travel the length of the leading edge before extinguishing at the rear corners of the cell (parts iv and v). This is followed by a transient decrease in membrane tension, allowing a new wave to form at the site of initial protrusion where VASP has once again accumulated (part v).

protrusion is extinguished at the rear corners of the cell. Inhibition of protrusion in the rear corners of the cell may be mediated by mature adhesions and myosin, both of which accumulate in the rear of the cell and may inhibit membrane protrusion by promoting actin network bundling, depolymerization, and/or retrograde flow [23, 40].

Numerical simulations of three versions of this model—a 1D model, a 2D model, and a dynamic leading-edge model (see Supplemental Information)—spontaneously exhibit traveling waves of protrusion (Figure 6B). Moreover, we varied the parameter that quantifies adhesion strength in our model and found that we were able to recapitulate our experimental measurements of adhesion-dependent changes in leading-edge dynamics. Specifically, at reduced adhesion strengths, the entire leading edge in our model protrudes at a constant rate (Figures 6Av and 6Bv), consistent with the rapidly migrating, smooth keratocytes we observed on surfaces coated with intermediate densities of RGD peptides (Figure 1). Consistent with the emergence of waving cells on surfaces coated with high densities of RGD peptides [8] (Figure 1), increasing the

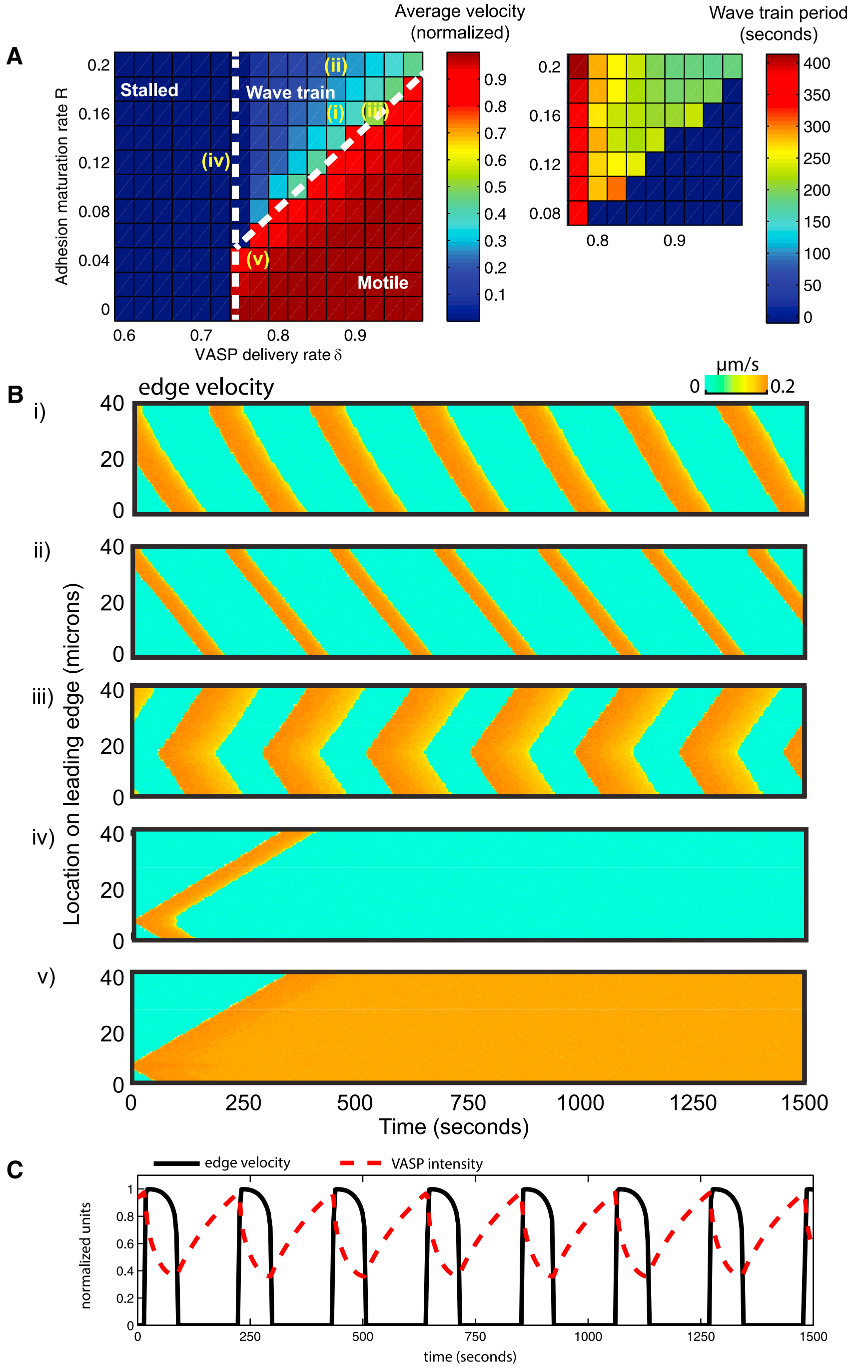

Figure 6. Model Simulations Recapitulate Adhesion- and VASP-Dependent Wave Generation

(A) Phase diagram showing average leading-edge velocity as a function of two model parameters, VASP delivery rate δ and adhesion maturation rate R. Dashed lines show predicted transitions between stalled, waving, and smooth motile leading edges. (i)–(v) correspond to the kymographs shown in (B). The inset to the right of the main figure shows the wave period in seconds for the region of parameter space exhibiting waves.

(B) Kymographs showing protrusion velocity along the leading edge over time; roman numbers correspond to values of δ and R shown in (A). Orange indicates protrusion; green indicates stalled regions.

(C) Time series of local concentration of VASP and protrusion velocity at a particular point on the leading edge in a simulated waving cell.

adhesion strength parameter results in waves of protrusion (Figures 6A and 6Bi–iii). Increasing the adhesion parameter even further increases the wave period while decreasing the fraction of the leading edge that protrudes (Figures 6A and 6B; compare i and ii), also consistent with our experimental results (Figures 1P, 2D, and 2J). In addition, we varied the parameter that quantifies the rate of VASP delivery to the leading edge and found that waving protrusion disappeared as VASP delivery increased (Figure 6A), consistent with the experimentally observed reduction of waving in cells overexpressing VASP (Figure 4).

Out of the three feedbacks on which the model is based, the local positive feedback between the branching rate and protrusion and negative feedback between VASP-accelerated protrusion and adhesion-mediated VASP depletion are essential for the excitable waves of protrusion. Without either of these feedbacks, protrusion can be either steady or bistable, but protrusion waves do not emerge (see Supplemental Information). Although the precise molecular mechanism underlying positive feedback between protrusion and the branching rate is uncertain, our model predicts that reducing the branching rate should diminish positive feedback with protrusion and, thus, abolish protrusion waves. Consistent with this, we found that inhibiting branching with CK666, a small-molecule inhibitor of Arp2/3, significantly reduced the number of waving cells (Figure S6). The third, global, feedback between the membrane tension and protrusion is not essential for the wave emergence but is necessary to make the wave pulses periodic: without this feedback, the next wave does not emerge at one end of the leading edge when the previous wave is extinguished at the opposite end, but rather the waves emerge at relatively random locations and times (see Supplemental Information).

VASP Localizes to the Leading Edge prior to the Initiation of Protrusion

In addition to recapitulating our experimental results, our model simulations also predict that VASP leading-edge localization should oscillate, with VASP most enriched at the leading edge prior to initiation of protrusion (Figure 6C). To test this, we examined the dynamic localization of VASP by measuring the intensity

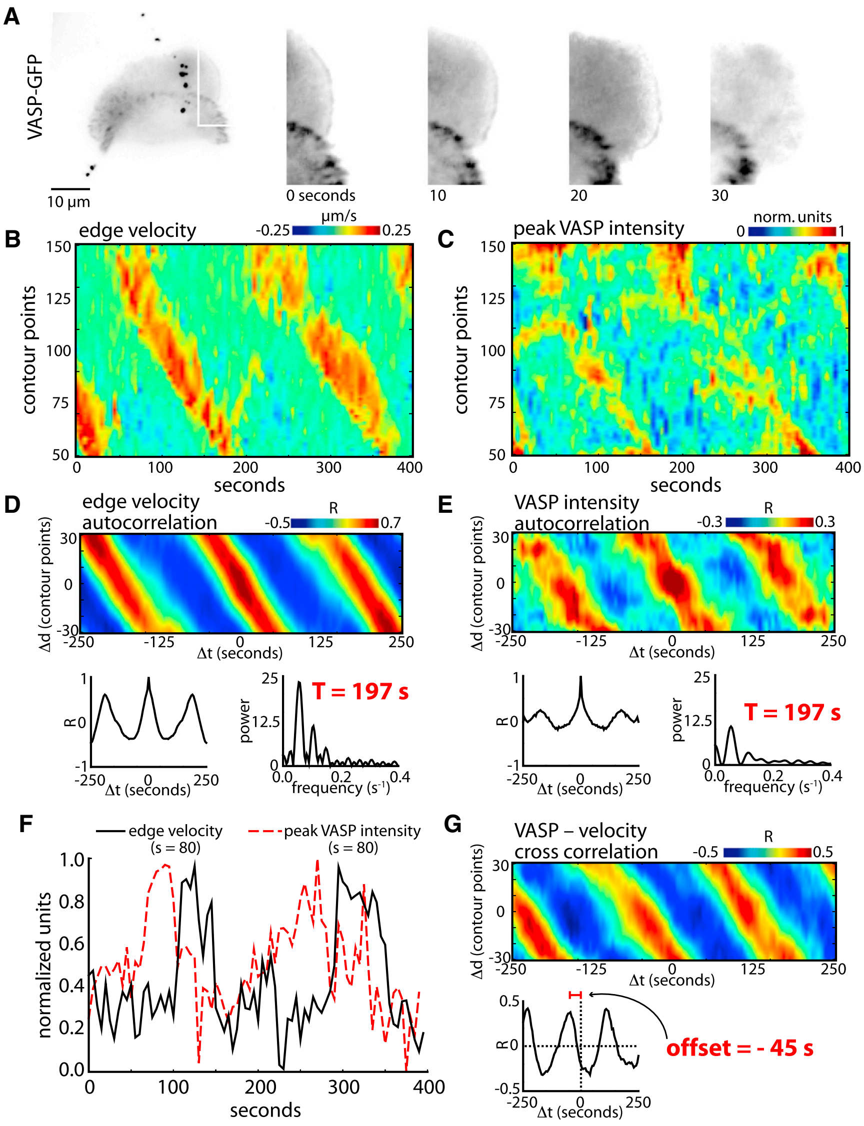

Figure 7. VASP Localization to the Leading Edge Increases prior to Protrusion Initiation

(A) Fluorescence images of a highly adhesive waving cell expressing VASP-GFP. The white box indicates the region enlarged in the images on the left.

(B) Edge velocity map.

(C) Peak VASP intensity map. The highest fluorescence intensity at each point along the cell boundary is plotted over time. Hot colors indicate high fluorescence intensities, and cold colors indicate low intensities.

(D and E) Edge velocity (D) and VASP intensity (E) autocorrelation maps. Autocorrelation coefficients for the indicated time (Δt) and contour position (Δd) offsets are plotted for the edge velocity and VASP intensity maps shown in (B) and (C). Hot colors indicate positive correlation, and cold colors indicate negative correlation. The graphs below the autocorrelation maps show the autocorrelation function at Δd = 0 (left) and the power spectrum of the autocorrelation function (right). Edge velocity and VASP intensity at the cell edge both oscillated with a period of 197 s.

(F) Velocity (black line) and VASP intensity (dashed red line) at the same point along the leading edge, plotted over time.

(G) Edge velocity and VASP-GFP cross-correlation map. Cross-correlation coefficients for the edge velocity and VASP intensity maps shown in (B) and (C) are plotted at the indicated time and distance offsets. The graph below the cross-correlation map shows the cross-correlation function at Δd = 0. The offset of −45 s indicates that VASP localization at the leading edge increases prior to protrusion of the leading edge.

See also Figures S6 and S7.

of GFP-VASP at all points along the cell perimeter, along with the edge velocity, in four waving cells (Figure 7). We found, first, that VASP intensity at the leading edge oscillated with the same period as the edge velocity (Figures 7D and 7E). To determine whether the oscillation of VASP localization is phase shifted relative to the oscillation of edge velocity, we calculated correlation coefficients for the edge velocity map and the GFP-VASP intensity map at different time and distance offsets (Figure 7G). GFP-VASP intensity increased prior to initiation of protrusion in all four cells, with time lags ranging from 5 s to 45 s (Figures 7F and 7G). To rule out the possibility that the measured changes in GFP-VASP intensity were due to oscillations in thickness of the leading edge, we measured edge intensities in cells transfected with GFP alone and found that GFP intensity at the leading edge oscillated in an irregular fashion and that intensity levels peaked after, rather than prior to, the initiation of protrusion (Figure S7). All together, these results are consistent with a model in which adhesion-dependent depletion of VASP results in traveling waves of protrusion.

DISCUSSION

We have presented a model in which traveling waves of protrusion in highly adherent keratocytes are driven by mechanical and biochemical feedback among adhesions, actin, VASP, and the cell membrane (Figure 5). In this model, tension in the membrane determines the critical actin barbed-end density required for protrusion initiation, and increasing or decreasing the amount of VASP moves the barbed-end density closer to or farther from this critical density, respectively. When the barbed-end density is sufficiently high, protrusion initiation sets off a positive feedback loop, with increased protrusion promoting increased actin branching and, thus, local actin barbed-end density. Protrusion waves propagate along the leading edge due to the branched architecture of the actin network, which results in lateral flow of actin barbed ends. Protrusion also triggers two negative feedback loops. First, fast, global negative feedback via a slight increase in membrane tension increases the critical barbed-end density for new protrusions, effectively limiting the cell to a single protrusion. Second, slow, local negative feedback with adhesions depletes VASP from the protruding edge of the cell, eventually reducing the density of barbed ends below the critical density and terminating protrusion behind the wave front. Our model and experimental data suggest that these feedback loops constitute an excitable system sufficient for the emergence of traveling waves of protrusion.

Cells exhibit considerable creativity in terms of the specific feedback loops underlying excitability [13]. For example, in addition to the feedback loops in our model, Arp2/3-actin-excitable feedbacks [6, 10], negative feedback from myosin contraction [4, 11], and signaling pacemakers based on Rho-GTPase pathways [7, 9, 41] have all been proposed to contribute to excitability. In principle, any positive and negative feedback loops could drive excitable actin dynamics, just as long as these feedback loops operate over the proper temporal and spatial scales; fast, local positive feedback combined with slow negative feedback drives excitability in many systems [13]. Interestingly, our model predicted that rapid and global negative feedback between actin polymerization and tension in the cell membrane is also essential for regular periodic traveling waves in highly adherent keratocytes (see Supplemental Experimental Procedures). Negative feedback between actin network dynamics and membrane tension has been demonstrated for steady-state keratocyte motility [36] and neutrophil migration [42]; further work is required to determine whether transient increases in membrane tension play a role in traveling waves.

Excitable actin dynamics are important not only at the leading edge of motile cells but also in sensitizing chemotactic pathways [41], regulating cell-cortex behavior in cytokinesis [22], and signaling in dendritic spines [43]. These and many other examples indicate that such dynamics are not exceptions but rather essential features of cell physiology. Moreover, waves of protrusion appear not only in in vitro 2D experiments: cells migrating through 3D ECM are guided by small and rapid traveling ''fins'' highly reminiscent of truncated keratocyte lamellipodia [44]. Thus, it is possible that the combination of mechanochemical feedbacks involving adhesions, actin, membrane, and regulatory proteins in keratocytes, which have extremely robust mechanisms for concentrating polymerization machinery to the leading edge, constitute a general conserved module underlying excitable actin dynamics.

EXPERIMENTAL PROCEDURES

Keratocyte Culture and Labeling

Experiments using live vertebrate animals, the Central American cichlid *Hypsophrys nicaraguensis*, were approved by the Stanford University Institutional Animal Care and Use Committee, protocol ID 10240. Keratocytes were cultured from *Hypsophrys nicaraguensis* scales as described previously [27]. Briefly, scales were sandwiched between two acid-washed coverslips and cultured in Leibovitz's Media (L-15) supplemented with 14.2 mM HEPES (pH 7.4), 10% fetal bovine serum (FBS), and 1% antibiotic-antimycotic at room temperature for 12–24 hr. Keratocytes were replated by trypsinization: cells were washed briefly with PBS and then treated with 0.1% PBS and 1 mM EDTA in PBS for 5 min. The trypsin was quenched with a 10-fold excess of culture media, and the cells were transferred directly to new surfaces and allowed to recover for 1 hr.

Alexa Fluor 546 phalloidin (AF546-phalloidin, Invitrogen) was used to label F-actin for fluorescent speckle microscopy (FSM), as previously described [45]. 2 nmol AF546-phalloidin were mixed with 7 μM deoxy-ATP (dATP), 7 μM deoxy-GTP, and 5 μM dexoy-CTP in double-distilled water (ddH_2O) for 15 min at room temperature to prevent phalloidin aggregation. The phalloidin mixture was electroporated into keratocytes using a small volume perfusion chamber with field stimulation (Warner Instruments) with three pulses at 180 V. Electroporated cells were allowed to recover for approximately 20 min before they were replated. VASP overexpression was performed by transfection, as previously described [27]. Keratocyte cultures were placed in Hank's balanced salt solution for fish, and ∼10 μg of either phosphorylated (p)EGFP-C1 or pEGFP-VASP plasmid DNA was added to the cultures immediately prior to electroporation. The cultures were allowed to recover in full media for 18–24 hr to allow for expression prior to replating and imaging.

Surface Preparation

The strength of cell-substrate adhesion was controlled by plating keratocytes on glass coverslips functionalized with either high or intermediate densities of RGD peptides. RGD density was controlled using RGD functionalized poly-L-lysine-graft-(polyethylene glycol) copolymers (PLL-PEG-RGD), as previously described [8]. Positively charged PLL polymers bind the negatively charged glass surface, PEG polymers passivate the surface—i.e., prevent the adsorption of serum proteins—and RGD peptides support cell adhesion via integrin receptors. Surfaces with different RGD densities were generated by dissolving PLL-PEG-RGD and PLL-PEG copolymers in PBS and mixing them at various ratios, to a total final concentration of 0.5 mg/mL. ''High'' adhesion surfaces were coated with 100% PLL-PEG-RGD (0.5 mg/mL), whereas ''intermediate'' adhesion surfaces were coated with solutions containing 2% PLL-PEG-RGD (0.01 mg/mL). Glass coverslips were washed with isopropanol and acetone and coated with PLL-PEG/PLL-PEG-RGD for 20 min at room temperature. The coverslips were washed extensively with ddH_2O and stored at 4°C for up to 24 hr prior to use. The PLL-PEG and PLL-PEG-RGD copolymers were synthesized as previously described [8].

Immunofluorescence

Indirect immunofluorescence was performed using a monoclonal mouse anti-vinculin antibody (hVIN-1, ab11194, Abcam). Cells were fixed at room temperature with 4% formaldehyde in 0.32 M sucrose in PBS for 15 min, permeabilized with 0.5% Triton X-100 for 10 min, and blocked with PBS-BT (3% BSA, 0.1% Triton X-100, and 0.02% sodium azide in PBS) for 30 min prior to incubation with primary antibody diluted in PBS-BT. F-actin was labeled with fluorescently conjugated phalloidin.

Microscopy

Live cells were imaged on an inverted microscope (Diaphot-300, Nikon) using a 40× NA 1.3 oil plan Fluor or a 60× NA 1.4 oil plan-Apo objective (Nikon). Epifluorescence images of fixed cells were aquired with an upright microscope (Axioplan 2; Carl Zeiss MicroImaging) using a 63× NA 1.4 oil plan Apochromat objective (Carl Zeiss MicroImaging). Images were collected with a cooled back-thinned charge-coupled device (CCD) camera (MicroMax 512BFT; Princeton Instruments) with a 2× optovar attached using MetaMorph software (Molecular Devices). Total internal reflection fluorescence (TIRF) images were acquired using an inverted microscope (AxioObserver; Carl Zeiss MicroImaging), a 100× NA 1.4 TIRF objective (Carl Zeiss MicroImaging), a 488-nm laser line, and a motorized TIRF slider (Zeiss). Images were collected with an electron microscopy (EM)-CCD camera (Hamamatsu) using AxioVision software (Zeiss).

Analysis of Protrusion Dynamics

Protrusion dynamics were measured from cell boundary contours as previously described [8, 46] Briefly, binary cell masks were manually extracted from phase images using the Quick Selection tool in Photoshop (Adobe). Celltool, open source Python code for quantifying cell shape [46], was used to extract polygonal cell outlines from the binary masks. The cell outlines were represented as 2D splines, which were then resampled at 200 evenly spaced points to generate the final contours. Cell boundary dynamics were then measured using custom Python code. Displacement vectors between polygons extracted from successive image frames were calculated for each point. The edge velocity at each point was calculated by dividing the component of the displacement vector normal to the cell edge by the time interval at which the images were acquired (5–10 s). Wave periods were measured by fast Fourier transform of the autocorrelation function of the edge velocity at the center of the leading edge (contour point 100).

Measurement of Actin Network Flow

Movement of the actin network at the leading edge was measured using an adaptive multi-frame correlation algorithm [23]. Briefly, we used five-frame averaging (10 s) and a correlation template between 11 pixels × 11 pixels and 21 pixels × 21 pixels. This method assumes steady-state movement of the actin network within the area of the correlation template over the duration of the temporal window, but the leading edge in keratocytes protrudes too quickly to meet this requirement. Thus, image sequences were converted from the laboratory frame of reference to a leading-edge frame of reference prior to flow tracking. The flow measurements were performed in the leading-edge frame of reference, and the resulting flow maps were then transformed back to the laboratory frame of reference. Phalloidin speckles were accentuated by applying a spatial band-pass filter to the images before flow tracking.

Mathematical Modeling

We used analytical and numerical analyses of partial differential equations for modeling; see Supplemental Experimental Procedures for details.

SUPPLEMENTAL INFORMATION

Supplemental Information includes Supplemental Experimental Procedures, fourteen figures, and two tables and can be found with this article online at http://dx.doi.org/10.1016/j.cub.2016.11.011.

AUTHOR CONTRIBUTIONS

E.L.B., J.A., J.A.T., and A.M. conceived and designed the experiments and the model. E.L.B. and S.S.L. performed the experiments. E.L.B. analyzed the experimental data. A.M. and J.A. developed the mathematical model and performed model simulations. E.L.B., J.A., A.M., and J.A.T. wrote the manuscript.

ACKNOWLEDGMENTS

This study was supported by NIH grant GM068952 (to A.M.), Stanford Medical Scientist Training Program NIH grant T32-GM007365 (to S.S.L.), and by the Stanford Center for Systems Biology (NIH grant P50-GM107615) and the Howard Hughes Medical Institute (to J.A.T.).

Received: April 20, 2016
Revised: August 26, 2016
Accepted: November 3, 2016
Published: December 8, 2016

REFERENCES

1. Ridley, A.J. (2011). Life at the leading edge. Cell *145*, 1012–1022.
2. Giannone, G., Dubin-Thaler, B.J., Döbereiner, H.-G., Kieffer, N., Bresnick, A.R., and Sheetz, M.P. (2004). Periodic lamellipodial contractions correlate with rearward actin waves. Cell *116*, 431–443.
3. Machacek, M., and Danuser, G. (2006). Morphodynamic profiling of protrusion phenotypes. Biophys. J. *90*, 1439–1452.
4. Burnette, D.T., Manley, S., Sengupta, P., Sougrat, R., Davidson, M.W., Kachar, B., and Lippincott-Schwartz, J. (2011). A role for actin arcs in the leading-edge advance of migrating cells. Nat. Cell Biol. *13*, 371–381.
5. Döbereiner, H.-G., Dubin-Thaler, B.J., Hofman, J.M., Xenias, H.S., Sims, T.N., Giannone, G., Dustin, M.L., Wiggins, C.H., and Sheetz, M.P. (2006). Lateral membrane waves constitute a universal dynamic pattern of motile cells. Phys. Rev. Lett. *97*, 038102.
6. Weiner, O.D., Marganski, W.A., Wu, L.F., Altschuler, S.J., and Kirschner, M.W. (2007). An actin-based wave generator organizes cell motility. PLoS Biol. *5*, e221.
7. Machacek, M., Hodgson, L., Welch, C., Elliott, H., Pertz, O., Nalbant, P., Abell, A., Johnson, G.L., Hahn, K.M., and Danuser, G. (2009). Coordination of Rho GTPase activities during cell protrusion. Nature *461*, 99–103.
8. Barnhart, E.L., Lee, K.-C., Keren, K., Mogilner, A., and Theriot, J.A. (2011). An adhesion-dependent switch between mechanisms that determine motile cell shape. PLoS Biol. *9*, e1001059.
9. Tkachenko, E., Sabouri-Ghomi, M., Pertz, O., Kim, C., Gutierrez, E., Machacek, M., Groisman, A., Danuser, G., and Ginsberg, M.H. (2011). Protein kinase A governs a RhoA-RhoGDI protrusion-retraction pacemaker in migrating cells. Nat. Cell Biol. *13*, 660–667.
10. Ryan, G.L., Petroccia, H.M., Watanabe, N., and Vavylonis, D. (2012). Excitable actin dynamics in lamellipodial protrusion and retraction. Biophys. J. *102*, 1493–1502.
11. Lou, S.S., Diz-Muñoz, A., Weiner, O.D., Fletcher, D.A., and Theriot, J.A. (2015). Myosin light chain kinase regulates cell polarization independently of membrane tension or Rho kinase. J. Cell Biol. *209*, 275–288.
12. Katsuno, H., Toriyama, M., Hosokawa, Y., Mizuno, K., Ikeda, K., Sakumura, Y., and Inagaki, N. (2015). Actin migration driven by directional assembly and disassembly of membrane-anchored actin filaments. Cell Rep. *12*, 648–660.
13. Allard, J., and Mogilner, A. (2013). Traveling waves in actin dynamics and cell motility. Curr. Opin. Cell Biol. *25*, 107–115.
14. Cirit, M., Krajcovic, M., Choi, C.K., Welf, E.S., Horwitz, A.F., and Haugh, J.M. (2010). Stochastic model of integrin-mediated signaling and adhesion dynamics at the leading edges of migrating cells. PLoS Comput. Biol. *6*, e1000688.
15. Doubrovinski, K., and Kruse, K. (2011). Cell motility resulting from spontaneous polymerization waves. Phys. Rev. Lett. *107*, 258103.
16. Ryan, G.L., Watanabe, N., and Vavylonis, D. (2012). A review of models of fluctuating protrusion and retraction patterns at the leading edge of motile cells. Cytoskeleton *69*, 195–206.
17. Enculescu, M., Sabouri-Ghomi, M., Danuser, G., and Falcke, M. (2010). Modeling of protrusion phenotypes driven by the actin-membrane interaction. Biophys. J. *98*, 1571–1581.
18. Peleg, B., Disanza, A., Scita, G., and Gov, N. (2011). Propagating cell-membrane waves driven by curved activators of actin polymerization. PLoS ONE *6*, e18635.
19. Carlsson, A.E. (2010). Dendritic actin filament nucleation causes traveling waves and patches. Phys. Rev. Lett. *104*, 228102.
20. Khamviwath, V., Hu, J., and Othmer, H.G. (2013). A continuum model of actin waves in Dictyostelium discoideum. PLoS ONE *8*, e64272.
21. Bernitt, E., Koh, C.G., Gov, N., and Döbereiner, H.-G. (2015). Dynamics of actin waves on patterned substrates: a quantitative analysis of circular dorsal ruffles. PLoS ONE *10*, e0115857.
22. Bement, W.M., Leda, M., Moe, A.M., Kita, A.M., Larson, M.E., Golding, A.E., Pfeuti, C., Su, K.-C., Miller, A.L., Goryachev, A.B., and von Dassow, G. (2015). Activator-inhibitor coupling between Rho signalling and actin assembly makes the cell cortex an excitable medium. Nat. Cell Biol. *17*, 1471–1483.
23. Wilson, C.A., Tsuchida, M.A., Allen, G.M., Barnhart, E.L., Applegate, K.T., Yam, P.T., Ji, L., Keren, K., Danuser, G., and Theriot, J.A. (2010). Myosin II contributes to cell-scale actin network treadmilling through network disassembly. Nature *465*, 373–377.
24. Ofer, N., Mogilner, A., and Keren, K. (2011). Actin disassembly clock determines shape and speed of lamellipodial fragments. Proc. Natl. Acad. Sci. USA *108*, 20394–20399.
25. Doubrovinski, K., and Kruse, K. (2008). Cytoskeletal waves in the absence of molecular motors. EPL *83*, 18003.
26. Whitelam, S., Bretschneider, T., and Burroughs, N.J. (2009). Transformation from spots to waves in a model of actin pattern formation. Phys. Rev. Lett. *102*, 198103.
27. Lacayo, C.I., Pincus, Z., VanDuijn, M.M., Wilson, C.A., Fletcher, D.A., Gertler, F.B., Mogilner, A., and Theriot, J.A. (2007). Emergence of large-scale cell morphology and movement from local actin filament growth dynamics. PLoS Biol. *5*, e233.
28. Ruoslahti, E., and Pierschbacher, M.D. (1987). New perspectives in cell adhesion: RGD and integrins. Science *238*, 491–497.

29. Slack-Davis, J.K., Martin, K.H., Tilghman, R.W., Iwanicki, M., Ung, E.J., Autry, C., Luzzio, M.J., Cooper, B., Kath, J.C., Roberts, W.G., and Parsons, J.T. (2007). Cellular characterization of a novel focal adhesion kinase inhibitor. J. Biol. Chem. *282*, 14845–14852.

30. Gupton, S.L., and Waterman-Storer, C.M. (2006). Spatiotemporal feedback between actomyosin and focal-adhesion systems optimizes rapid cell migration. Cell *125*, 1361–1374.

31. Kuo, J.C., Han, X., Hsiao, C.T., Yates, J.R., 3rd, and Waterman, C.M. (2011). Analysis of the myosin-II-responsive focal adhesion proteome reveals a role for β-Pix in negative regulation of focal adhesion maturation. Nat. Cell Biol. *13*, 383–393.

32. Dubin-Thaler, B.J., Hofman, J.M., Cai, Y., Xenias, H., Spielman, I., Shneidman, A.V., David, L.A., Döbereiner, H.-G., Wiggins, C.H., and Sheetz, M.P. (2008). Quantification of cell edge velocities and traction forces reveals distinct motility modules during cell spreading. PLoS ONE *3*, e3735.

33. Keren, K., Pincus, Z., Allen, G.M., Barnhart, E.L., Marriott, G., Mogilner, A., and Theriot, J.A. (2008). Mechanism of shape determination in motile cells. Nature *453*, 475–480.

34. Bear, J.E., Svitkina, T.M., Krause, M., Schafer, D.A., Loureiro, J.J., Strasser, G.A., Maly, I.V., Chaga, O.Y., Cooper, J.A., Borisy, G.G., and Gertler, F.B. (2002). Antagonism between Ena/VASP proteins and actin filament capping regulates fibroblast motility. Cell *109*, 509–521.

35. Hansen, S.D., and Mullins, R.D. (2010). VASP is a processive actin polymerase that requires monomeric actin for barbed end association. J. Cell Biol. *191*, 571–584.

36. Lieber, A.D., Yehudai-Resheff, S., Barnhart, E.L., Theriot, J.A., and Keren, K. (2013). Membrane tension in rapidly moving cells is determined by cytoskeletal forces. Curr. Biol. *23*, 1409–1417.

37. Choi, C.K., Vicente-Manzanares, M., Zareno, J., Whitmore, L.A., Mogilner, A., and Horwitz, A.R. (2008). Actin and α-actinin orchestrate the assembly and maturation of nascent adhesions in a myosin II motor-independent manner. Nat. Cell Biol. *10*, 1039–1050.

38. Anderson, K.I., and Cross, R. (2000). Contact dynamics during keratocyte motility. Curr. Biol. *10*, 253–260.

39. Barnhart, E.L., Allen, G.M., Jülicher, F., and Theriot, J.A. (2010). Bipedal locomotion in crawling cells. Biophys. J. *98*, 933–942.

40. Reymann, A.C., Boujemaa-Paterski, R., Martiel, J.L., Guérin, C., Cao, W., Chin, H.F., De La Cruz, E.M., Théry, M., and Blanchoin, L. (2012). Actin network architecture can determine myosin motor activity. Science *336*, 1310–1314.

41. Huang, C.-H., Tang, M., Shi, C., Iglesias, P.A., and Devreotes, P.N. (2013). An excitable signal integrator couples to an idling cytoskeletal oscillator to drive cell migration. Nat. Cell Biol. *15*, 1307–1316.

42. Houk, A.R., Jilkine, A., Mejean, C.O., Boltyanskiy, R., Dufresne, E.R., Angenent, S.B., Altschuler, S.J., Wu, L.F., and Weiner, O.D. (2012). Membrane tension maintains cell polarity by confining signals to the leading edge during neutrophil migration. Cell *148*, 175–188.

43. Ramirez, S.A., Raghavachari, S., and Lew, D.J. (2015). Dendritic spine geometry can localize GTPase signaling in neurons. Mol. Biol. Cell *26*, 4171–4181.

44. Guetta-Terrier, C., Monzo, P., Zhu, J., Long, H., Venkatraman, L., Zhou, Y., Wang, P., Chew, S.Y., Mogilner, A., Ladoux, B., and Gauthier, N.C. (2015). Protrusive waves guide 3D cell migration along nanofibers. J. Cell Biol. *211*, 683–701.

45. Yam, P.T., Wilson, C.A., Ji, L., Hebert, B., Barnhart, E.L., Dye, N.A., Wiseman, P.W., Danuser, G., and Theriot, J.A. (2007). Actin-myosin network reorganization breaks symmetry at the cell rear to spontaneously initiate polarized cell motility. J. Cell Biol. *178*, 1207–1221.

46. Pincus, Z., and Theriot, J.A. (2007). Comparison of quantitative methods for cell-shape analysis. J. Microsc. *227*, 140–156.

Current Biology, Volume *27*

Supplemental Information

Adhesion-Dependent Wave Generation in Crawling Cells

Erin L. Barnhart, Jun Allard, Sunny S. Lou, Julie A. Theriot, and Alex Mogilner

Figure S1

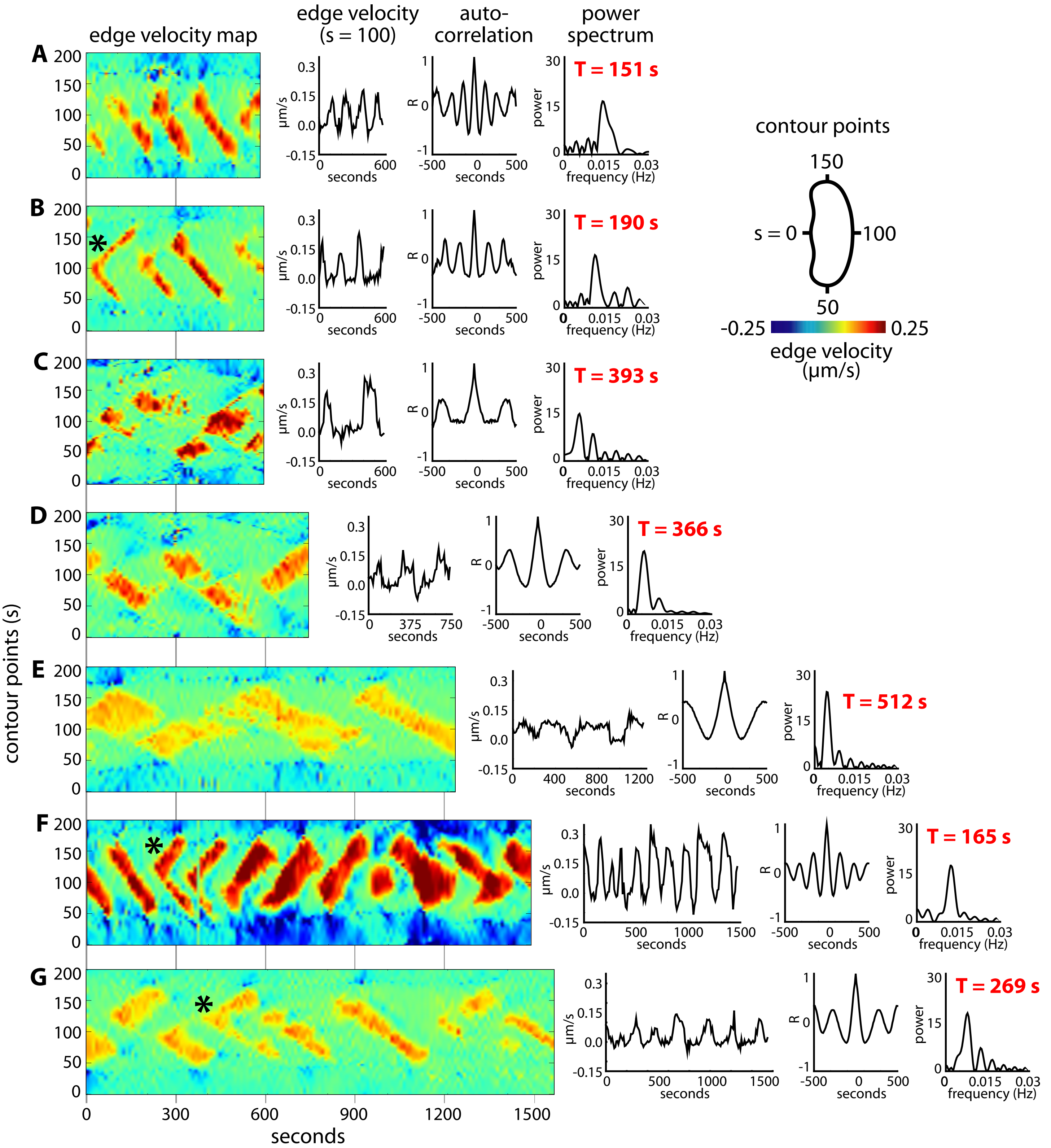
edge velocity map
edge velocity (s = 100)
auto-correlation
power spectrum
A
B
C
D
E
F
G
T = 151 s
T = 190 s
T = 393 s
T = 366 s
T = 512 s
T = 165 s
T = 269 s
contour points (s)
seconds
µm/s
R
power
frequency (Hz)
0
300
600
900
1200
1500
200
150
100
50
0.3
0.15
0.0
-0.15
1
-1
-500
500
30
15
0.015
0.03
375
750
400
800
1000
contour points
s = 0
-0.25
0.25
edge velocity
(µm/s)

Figure S2

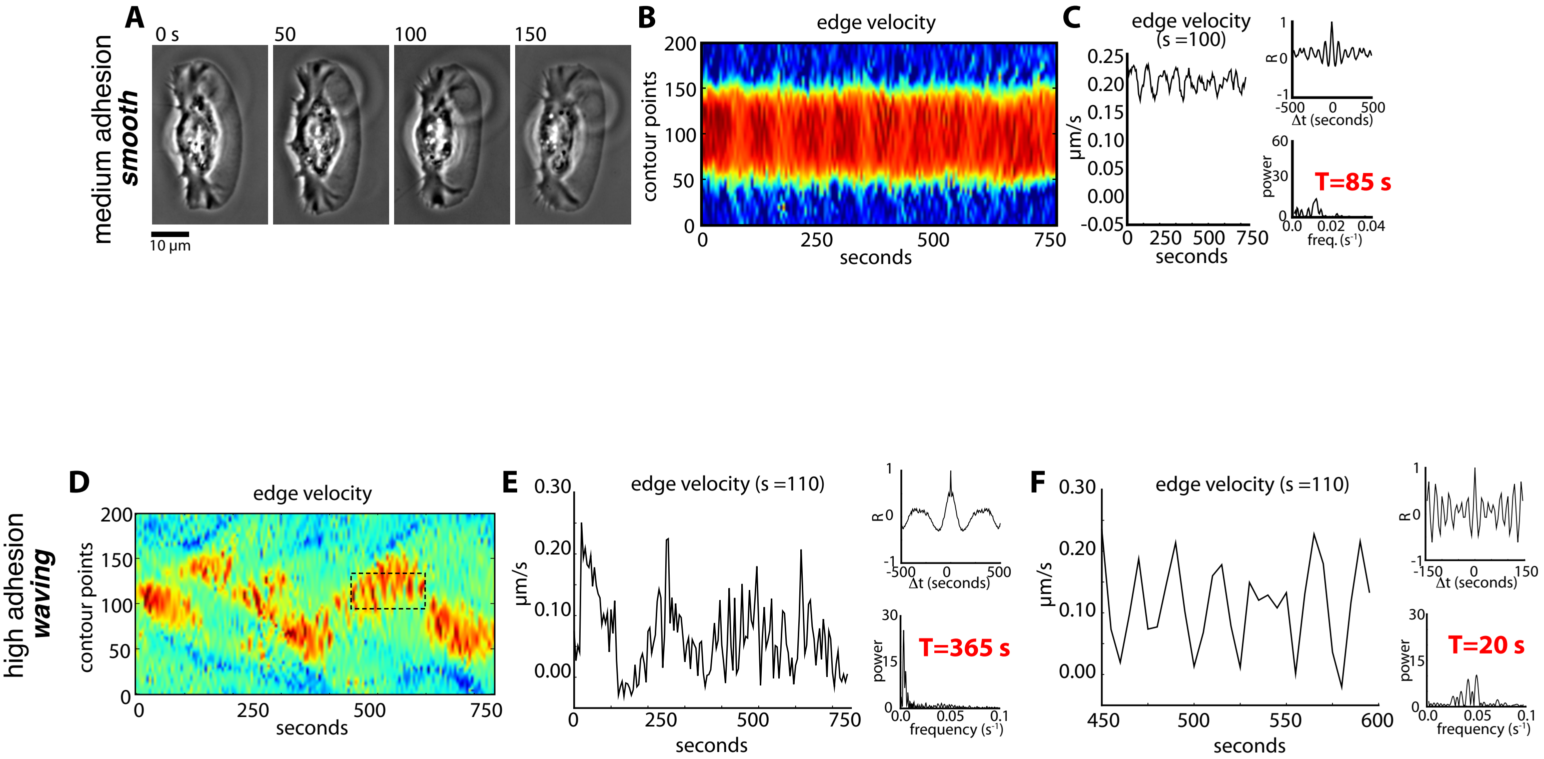
medium adhesion
smooth
A
0 s
50
100
150
10 µm
B
edge velocity
200
150
100
50
0
contour points
0
250
500
750
seconds
C
edge velocity
(s =100)
0.25
0.20
0.15
0.10
0.05
0.00
-0.05
µm/s
0
250
500
750
seconds
1
R 0
-1
-500
0
500
Δt (seconds)
60
30
0
power
0.0
0.02
0.04
freq. (s⁻¹)
T=85 s
high adhesion
waving
D
edge velocity
200
150
100
50
0
contour points
0
250
500
750
seconds
E
0.30
edge velocity (s =110)
0.20
0.10
0.00
µm/s
0
250
500
750
seconds
1
R 0
-1
-500
0
500
Δt (seconds)
30
15
0
power
0.0
0.05
0.1
frequency (s⁻¹)
T=365 s
F
0.30
edge velocity (s =110)
0.20
0.10
0.00
µm/s
450
500
550
600
seconds
1
R 0
-1
-150
0
150
Δt (seconds)
30
15
0
power
0.0
0.05
0.1
frequency (s⁻¹)
T=20 s

Figure S3

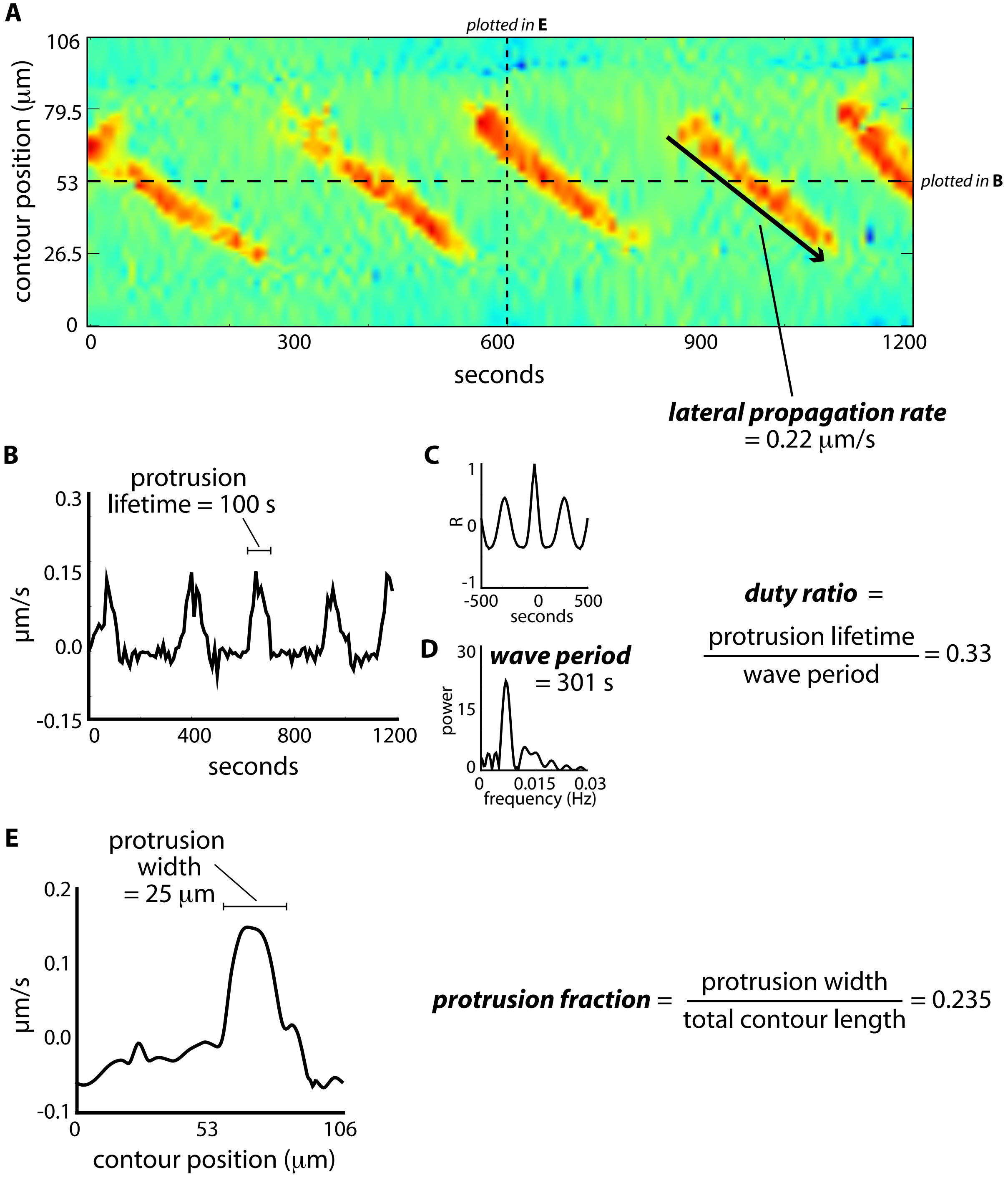

lateral propagation rate = 0.22 μm/s

wave period = 301 s

$$\textbf{\textit{duty ratio}} = \frac{\text{protrusion lifetime}}{\text{wave period}} = 0.33$$

$$\textbf{\textit{protrusion fraction}} = \frac{\text{protrusion width}}{\text{total contour length}} = 0.235$$

Figure S4

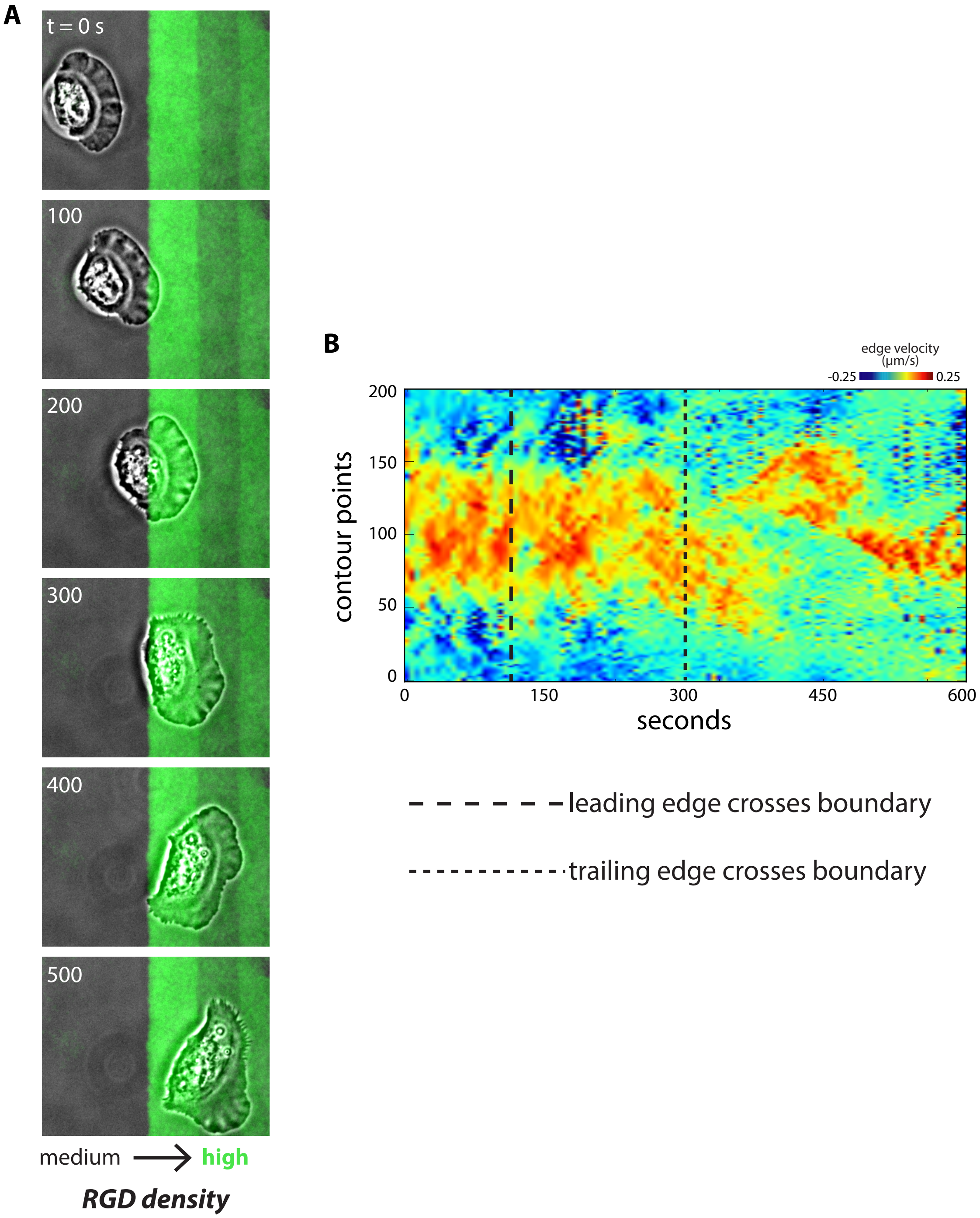
A
t = 0 s
100
200
300
400
500
medium
high
RGD density
B
edge velocity (µm/s)
-0.25
0.25
200
150
100
50
0
contour points
0
150
300
450
600
seconds
leading edge crosses boundary
trailing edge crosses boundary

Figure S5

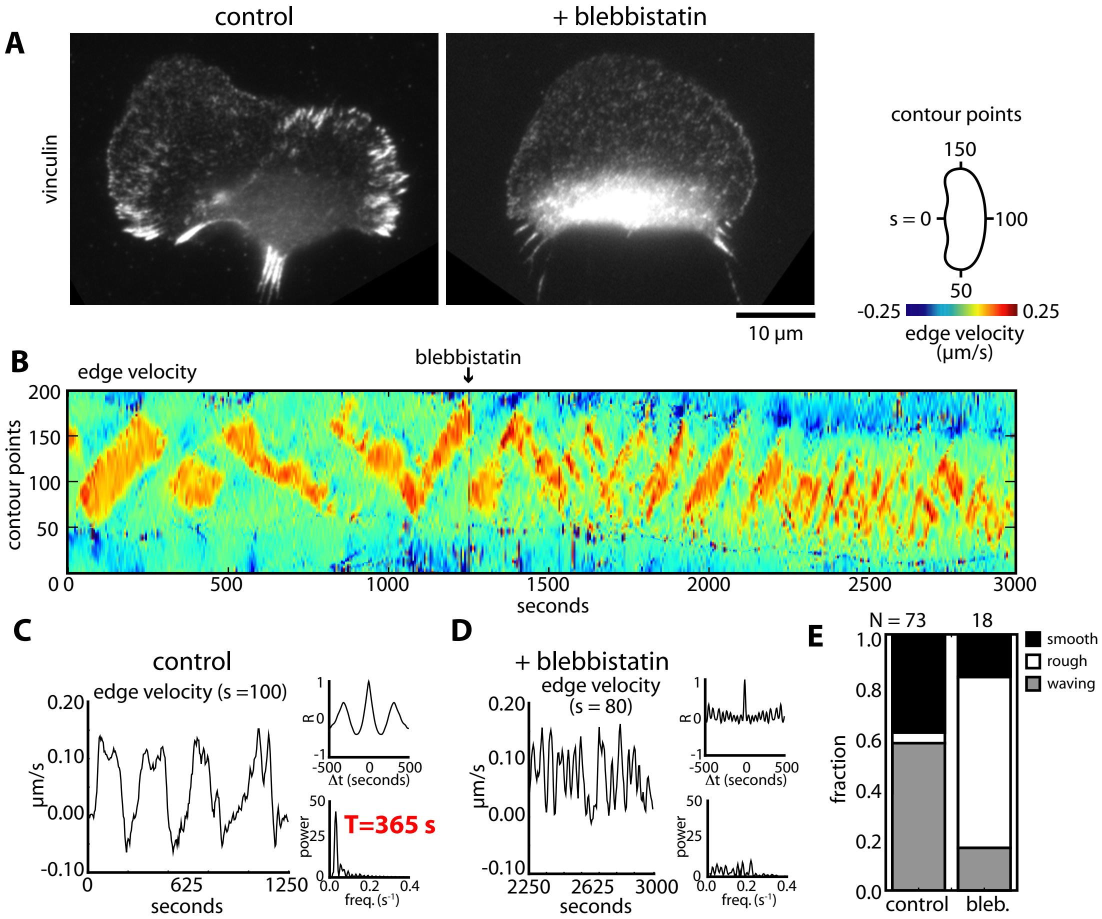
A
control
+ blebbistatin
vinculin
10 μm
contour points
150
s = 0
100
50
-0.25
0.25
edge velocity (μm/s)
B
edge velocity
blebbistatin
200
150
100
50
0
contour points
0
500
1000
1500
2000
2500
3000
seconds
C
control
edge velocity (s =100)
0.20
0.10
0.00
-0.10
μm/s
0
625
1250
seconds
1
R 0
-1
-500
0
500
Δt (seconds)
50
power 25
0
0.0
0.2
0.4
freq. (s⁻¹)
T=365 s
D
+ blebbistatin
edge velocity (s = 80)
0.20
0.10
0.00
-0.10
μm/s
2250
2625
3000
seconds
1
R 0
-1
-500
0
500
Δt (seconds)
50
power 25
0
0.0
0.2
0.4
freq. (s⁻¹)
E
N = 73
18
1.0
0.8
0.6
0.4
0.2
0.0
fraction
control
bleb.
smooth
rough
waving

Figure S6

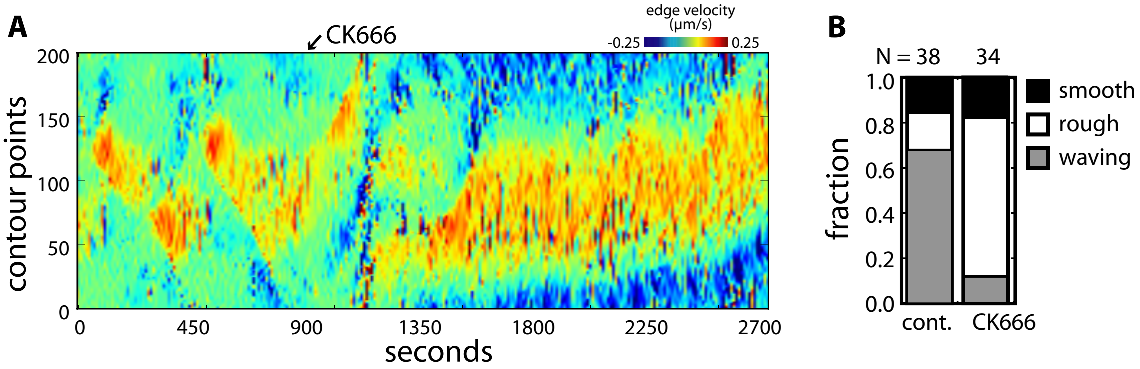
A
CK666
edge velocity (μm/s)
-0.25
0.25
contour points
200
150
100
50
0
0
450
900
1350
1800
2250
2700
seconds
B
N = 38
34
fraction
1.0
0.8
0.6
0.4
0.2
0.0
cont.
CK666
smooth
rough
waving

Figure S7

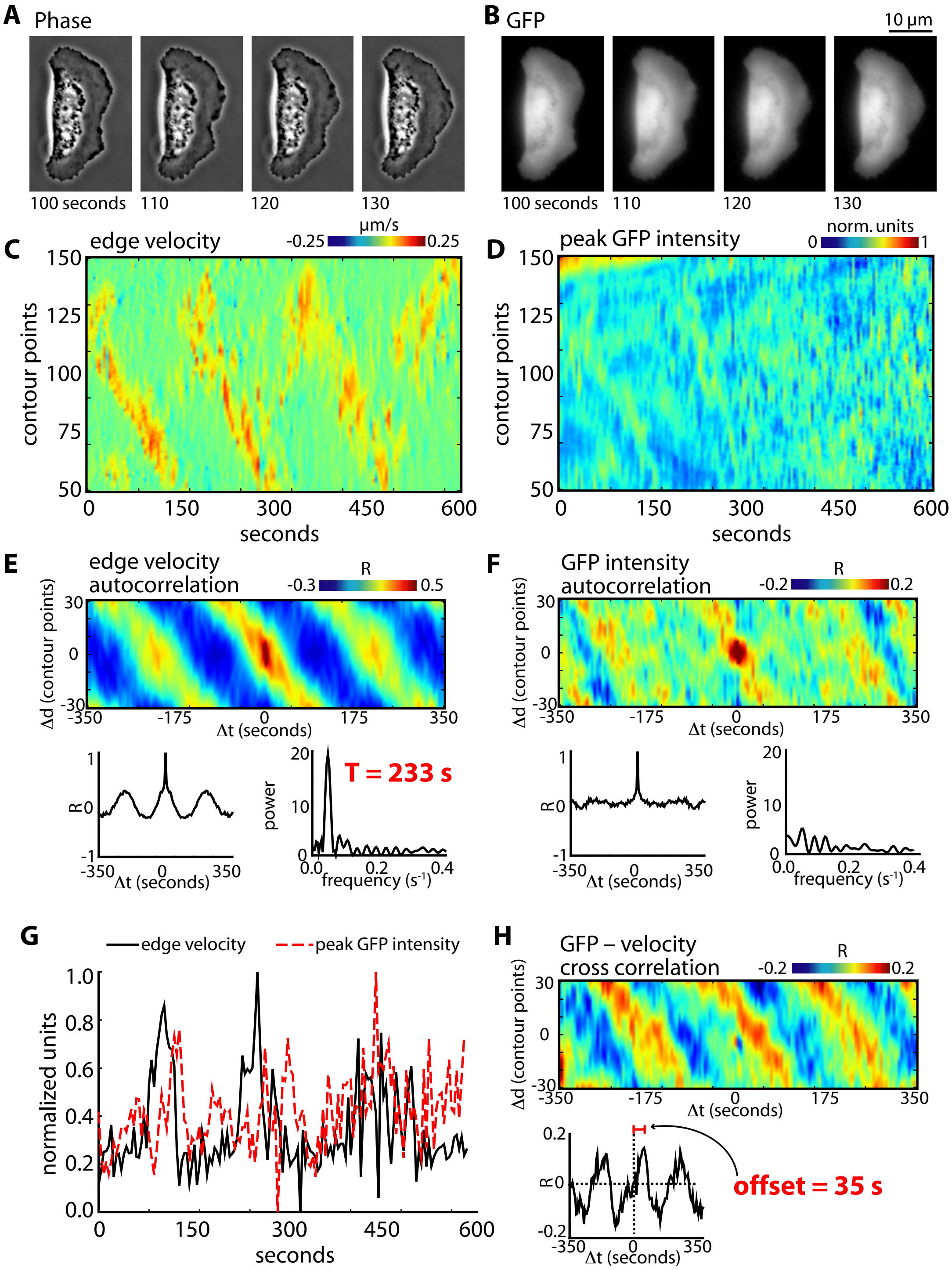
A
Phase
100 seconds
110
120
130
B
GFP
10 μm
100 seconds
110
120
130
C
edge velocity
μm/s
-0.25
0.25
contour points
150
125
100
75
50
0
150
300
450
600
seconds
D
peak GFP intensity
norm. units
0
1
contour points
150
125
100
75
50
0
150
300
450
600
seconds
E
edge velocity autocorrelation
R
-0.3
0.5
Δd (contour points)
30
0
-30
-350
-175
0
175
350
Δt (seconds)
R
1
0
-1
-350
0
350
Δt (seconds)
power
20
10
0
0.0
0.2
0.4
frequency (s⁻¹)
T = 233 s
F
GFP intensity autocorrelation
R
-0.2
0.2
Δd (contour points)
30
0
-30
-350
-175
0
175
350
Δt (seconds)
R
1
0
-1
-350
0
350
Δt (seconds)
power
20
10
0
0.0
0.2
0.4
frequency (s⁻¹)
G
edge velocity
peak GFP intensity
normalized units
1.0
0.8
0.6
0.4
0.2
0.0
0
150
300
450
600
seconds
H
GFP – velocity cross correlation
R
-0.2
0.2
Δd (contour points)
30
0
-30
-350
-175
0
175
350
Δt (seconds)
R
0.2
0
-0.2
-350
0
350
Δt (seconds)
offset = 35 s

Supplemental Figure Legends

Figure S1: Traveling waves in highly adherent keratocytes. Edge velocity maps and plots of leading edge velocity, the velocity autocorrelation function, and the power spectrum of the autocorrelation function for several highly adherent keratocytes that exhibit traveling waves. In most cases, protrusion initiates at one side of the leading edge and then proceeds along the length of the leading edge; the black asterix in parts B, F, and G indicate rare protrusions that initiated near the center of the leading edge, with protrusion then proceeding in both directions along the leading edge away from the site of initiation. In all cases, protrusion waves terminate at the rear corners of the cell (contour points 50 and 150). See also Figure 1 in the main text.

Figure S2: High frequency, low amplitude oscillations. A-C: Synchronous leading edge oscillations in a smooth cell. Phase images (A), edge velocity map (B), and leading edge velocity (C) for a cell plated on a surface coated with an intermediate density of RGD peptides (medium adhesion). The leading edge in this cell exhibits synchronous oscillation of the entire, smooth leading edge, as indicated by the peak in the power spectrum that correspond to an oscillation period of 85 seconds. D-F: High frequency oscillations on top of protrusion waves. Edge velocity map (D) and leading edge velocities (E-F) for a waving cell plated on a surface coated with a high density of RGD peptides. The time window plotted in part f is indicated by the dashed box on the edge velocity map. The cell exhibits both low frequency traveling waves (E, T = 365 seconds), and high frequency oscillations (F, T ~20 seconds). The insets in parts c, e and f are the leading edge velocity autocorrelation function (top) and the power spectrum of the autocorrelation function (bottom). See also Figure 1 in the main text.

Figure S3: Quantitative wave parameters. A: Edge velocity map. The rate of lateral propagation of the wave along the front of the cell was measured from the edge velocity map, as indicated by the arrow. B: Velocity of the leading edge, at the contour point indicated by the dashed line in part a, plotted versus time. The lifetime for a particular protrusion – the amount of time the protrusion rate at a particular contour point is greater than zero – is indicated by the bracket. C-D: Velocity autocorrelation (C) and power spectrum of the autocorrelation function (D). The wave period is measured from the power spectrum. The duty ratio is defined as the protrusion lifetime divided by the wave period. E: The velocity of the cell boundary at a particular point in time, indicated by the dashed line in part a, plotted versus position along the cell boundary. The width of the protrusion – the length of the cell boundary protruding at this particular point in time – is indicated by the bracket. The protrusion fraction is defined as the protrusion width divided by the total contour length. The parameters plotted for populations of cells in Figures 1 and 2 in the main text are indicated in bold, italicized text.

Figure S4: Traveling waves emerge in cells crawling on micropatterned surfaces. A cell was imaged crawling on a micropatterned surface as it crossed from a region patterned with an intermediate density of RGD peptides to a region patterned with a high density of RGD peptides. A: Phase images. The region patterned with a high density of RGD peptides is psuedocolored green. B: Edge velocity map. The dashed lines indicate when the cell's leading and trailing edges crossed the boundary from intermediate to high RGD densities. See also Figure 1 in the main text.

Figure S5. Myosin inhibition prevents adhesion maturation and abolishes waving. A: Images of cells plated on high adhesion strength surfaces and immunolabeled for vinculin. Adhesion size is reduced in cells treated with the myosin II inhibitor blebbistatin (left), relative to control cells (right). B-D: Edge velocity map (B) and velocity of the center of the leading edge for a waving cell before (C) and after (D) treatment with blebbistatin. The upper insets in C and D are the autocorrelation functions for the edge velocity, and the lower insets are the power spectrums of the autocorrelation functions. E: The fraction of waving, noisy, and smooth cells in populations of cells plated on high adhesion strength surfaces and treated with blebbistatin; the control data from Figure 1M is plotted again here for ease of comparison. See also Figure 2 in the main text.

Figure S6. Arp2/3 inhibition abolishes waving. Cells plated on surfaces coated with high densities of RGD peptides were treated with 100µM of the Arp2/3 small molecule inhibitor, CK666. A: Edge velocity map. The inhibitor was added at t = 900 seconds, and the cells switched from waving to a rough leading edge phenotype. B: Leading edge phenotypes. The fraction of waving, rough, and smooth cells before and after treatment with CK666. See also Figure 7 in the main text.

Figure S7. Leading edge thickness peaks after the onset of protrusion in waving cells. Phase (A) and epifluorescence (B) images of a highly adhesive, waving cell expressing GFP. C: Edge velocity map. D: Peak GFP intensity map. The highest fluorescence intensity at each point along the cell boundary is plotted over time. Hot colors indicate high fluorescence intensities and cold colors indicate low intensities. E-F: Edge velocity (E) and VASP intensity (F) autocorrelation maps. Autocorrelation coefficients for the indicated time (Δt) and contour position (Δd) offsets are plotted for the edge velocity and GFP intensity maps shown in parts C and D. Hot colors indicate positive correlation, and cold colors indicate negative correlation. The graphs below the autocorrelation maps show the autocorrelation function at $\Delta d=0$ (left) and the power spectrum of the autocorrelation function (right). Whereas edge velocity oscillated with a period of 233 seconds, GFP intensities exhibited irregular oscillations. G: Velocity (black line) and GFP intensity (dashed red line) at the same point along the leading edge, plotted over time. H: Edge velocity and GFP cross correlation map. Cross correlation coefficients for the edge velocity and VASP intensity maps shown in parts C and D are plotted at the indicated time and distance offsets. The graph below the cross correlation map shows the cross correlation function at $\Delta d=0$. The offset of +35 seconds indicates that GFP localization at the leading edge increases after protrusion of the leading edge. See also Figure 7 in the main text.

Mathematical model of traveling waves in the keratocyte leading edge

1 Basic model equations and assumptions

The leading edge is parametrized by $0 < x < l$, where l is the total length of the leading edge. The length $l \approx 40\,\mu$m [S12] is much longer than its width $w \approx 1\,\mu$m [S4], and we therefore formulate the model in one spatial dimension. Along the leading edge, we track the following densities: Actin filaments barbed ends at the leading edge, $b(x,t)$; nascent and mature adhesions $n(x,t)$, $m(x,t)$; and VASP, which is either cytosolic, or on barbed ends, or in mature adhesions: a_c, a_b, a_m. We also track an edge velocity at every point along the leading edge, $v(x,t)$. The model is summarized in the Fig. 5 of the main text. The equations governing the dynamics are described in this section. Parameters for the model are summarized in Table S1.

Actin barbed-end dynamics

- Branching rate depends on protrusion velocity, $\beta = \beta_0 + \beta_1 v$. This assumption reflects the distinct architecture of dendritic actin at the leading edge, depending on protrusion state [S3].
- Capping occurs at rate γ which is reduced by the local VASP concentration $\gamma = \gamma_0/(1 + a_b/a_0)$, where a_b is the local concentration of VASP currently on barbed ends. The uncapped barbed ends remain at the leading edge, independent of growth velocity because if they are stationary, so is the leading edge, whereas if they are polymerizing, the leading edge is moving forward with them. When an uncapped barbed end is capped, it is immediately removed from the edge. Under these assumptions, capping dynamics are independent of polymerization velocity.
- Polymerization at barbed-ends results in flow along the leading edge, described by the term $\phi(x,t)$, defined below.

The resulting dynamics are described by the equation:

$$\frac{\partial b}{\partial t} = \beta - \gamma b + \underbrace{\phi(x,t)}_{\text{lateral flow}} + \xi_t. \tag{1}$$

To break symmetry, we add a small noise term ξ_t, corresponding to, e.g., inhomogeneity in the substrate and stochasticity in the biochemical interactions, to the above equation through a Wiener process [S23] whose magnitude is $< 10^{-3}$ relative to the other terms. The effect of larger noise is discussed below in Model Variants.

Adhesions

- Nascent adhesion formation depends on the presence of barbed-ends [S4]; in the model, the source term is proportional to the barbed-end density, with ν^+ as proportionality coefficient.
- Nascent adhesions mature at rate μ and disassemble at rate ν^-. As we show below, the nascent adhesions dynamics formation, disassembly and maturation are sufficiently fast that they dominate the substrate-adhesion-based transport.

- Mature adhesions are removed by two processes: they decay with timescale $\tau_m \approx 30\,\mathrm{s}$ [S4]. They also drift away from the leading edge of width w at speed v during protrusion, since adhesions are mostly stationary in the frame of reference of the substrate [S4].

The resulting adhesion dynamics equations are:

$$\frac{\partial n}{\partial t} = \nu^+ b - (\nu^- + \mu)n \tag{2}$$

$$\frac{\partial m}{\partial t} = \mu n - (1/\tau_m + v/w)m \tag{3}$$

VASP dynamics

The local VASP concentration in each of the three compartments (cytosol, barbed-ends, mature adhesions) changes according to the following equation:

$$\frac{\partial}{\partial t}\begin{bmatrix} a_b \\ a_c \\ a_m \end{bmatrix} = EX \cdot \begin{bmatrix} a_b \\ a_c \\ a_m \end{bmatrix} + \begin{bmatrix} \delta \\ 0 \\ 0 \end{bmatrix} - \begin{bmatrix} 0 \\ D/w^2 + v/w \\ v/w \end{bmatrix} \cdot \begin{bmatrix} a_b \\ a_c \\ a_m \end{bmatrix}. \tag{4}$$

Below we describe the assumptions that lead to each term in the above equation.

- The matrix

$$EX = \begin{bmatrix} -k_{bc} & k_{cb}b & 0 \\ +k_{bc} & -(k_{cb}b + k_{cm}m) & +k_{mc} + 1/\tau_m \\ 0 & k_{cm}m & -k_{mc} - 1/\tau_m \end{bmatrix} \tag{5}$$

  describes the exchange between the three compartments. The terms involving τ_m describe the release of VASP from mature adhesions as they turn over. Sequestration of VASP into mature adhesions was observed in Lacayo et al. [S15] and Bear and Gertler [S2]. The exchange rates are mostly unmeasured, although Hansen and Mullins [S10] estimate $k_{ac} \approx 0.7\,\mathrm{s}^{-1}$.

- VASP is delivered by an unspecified process to the leading edge at a constant delivery rate δ. Recent evidence [S10] suggests VASP is delivered to barbed-ends by binding laterally along actin filaments and then undergoing 1D diffusion until either dissociation or encountering the barbed-end, after which it tracks along with the barbed-end.

- VASP is removed by several processes: adhesion-bound VASP are convected away by protrusion (last term in a_m equation), since adhesions are mostly stationary in the lab frame [S4]. Cytosolic VASP diffuses away from the leading edge (D/w^2 term in a_c equation). This term assumes that VASP concentration is much larger near the leading edge than further back in the lamellipod, in agreement with observations [S2]. Note that VASP is tetrameric [S10], suggesting a slow diffusion coefficient D, which scales linearly with protein size [S11]. In the following we assume $D = 0.2\,\mu\mathrm{m}^2/\,\mathrm{s}$. The v/w term in the a_c equation describes a flow of the cytosolic fluid, which carries VASP with it. If cytosolic fluid is stationary in the lab frame, cytosolic VASP will also be convected away by protrusion, as described in the equation. We discuss alternate assumptions about cytosolic flow in the section Model Variants, below.

- VASP lateral diffusion is negligible. We expect this to be a valid approximation by scaling arguments (the local concentration of VASP, as we observe experimentally, varies over the wavelength of $\approx 10\,\mu\mathrm{m}$ and the waves cycle with a timescale of $\sim 100\,\mathrm{s}$, implying a characteristic diffusion coefficient of $D \sim 1\,\mu\mathrm{m}^2/\,\mathrm{s}$, supporting the assumption above about the value of the diffusion coefficient in the model). Nonetheless, to more carefully examine the consequences of this simplifying assumption, in Sec. 5 below, we construct a more complex model and remove this assumption, including full diffusion throughout the entire lamellipodium. As discussed in that section, we find the same behavior as in this simplified model.

Actin polymerization, protrusion velocity and membrane tension

The velocity of the edge, $v(x,t)$, exhibits a switch-like transition with increasing barbed-end density [S12],

$$v = \begin{cases} v_0\left(1-(\Theta/(F_{\text{stall}}b))^8\right) & b > \Theta/F_{\text{stall}} \\ 0 & b < \Theta/F_{\text{stall}} \end{cases} \tag{6}$$

where v_0 is the free polymerization rate, F_{stall} is the stall force for individual filaments and Θ is the membrane tension. The force-velocity relation Eq. 6 is an empirical relation describing the complex interaction of a population of polymerizing barbed-ends, individually acting as Brownian ratchets [S18] and has been used in several studies [S1, S12].

Membrane tension is a cell-wide property that equilibrates quickly throughout the cell [S21, S26]. In keratocytes, it has been estimated to be on the order of $100\,\text{pN}/\,\text{nm}$ [S16]. It was shown in [S16] that the membrane tension increases when the actin polymerization grows, and filaments stretch the plasma membrane from within. Thus, we are making a simple assumption that the membrane tension Θ increases with increasing velocity as a step function:

$$\Theta = \begin{cases} \Theta_0 & v_r = 0 \\ \Theta_0(1+E) & v_r > 0 \end{cases} \tag{7}$$

The average protrusion rate v_r is defined as:

$$v_r = \frac{1}{l}\int_0^x v(x)dx, \tag{8}$$

We use a small fractional increase in membrane tension when protrusion is present, $E = 0.1$, based on the data in [S16].

Lateral protrusion

Actin barbed ends polymerize in a wide range of directions, leading to both lateral flow of barbed-ends, and protrusion (discussed next section). Locally, there are two subpopulations of actin filaments which point ±35° relative to the leading edge [S19], and which therefore polymerize either left or right at rates $v(x,t)\cdot\cos 35°$. Branching associated with one subpopulation creates a new barbed-end in the opposite subpopulation. This fact leads to a two-subpopulation model for barbed-ends used in Keren et al. [S12], Lacayo et al. [S15]:

$$\frac{\partial b_l}{\partial t} = -\cos 35°\frac{\partial}{\partial x}v(x,t)b_l + \beta\left(\frac{b_r-b_l}{b_r+b_l}\right) - \gamma \tag{9}$$

$$\frac{\partial b_r}{\partial t} = +\cos 35°\frac{\partial}{\partial x}v(x,t)b_r + \beta\left(\frac{b_l-b_r}{b_r+b_l}\right) - \gamma. \tag{10}$$

However, on length scales $\gg v/\beta$, it is sufficient to track the total density $b(x,t) = b_l(x,t) + b_r(x,t)$, which approximately obeys

$$\frac{\partial b}{\partial t} = \beta - \gamma b + (\cos 35°)\frac{\partial}{\partial x}\left(\frac{v^2}{2\gamma}\frac{\partial b}{\partial x}\right). \tag{11}$$

Derivation of this diffusion-like transport equation is based on standard methods of applied mathematics [S6] and was done in Lacayo et al. [S15].

Boundary conditions.

We explored two main types of boundary conditions for the growing barbed-ends when they reach either left or right corners of the leading edge (at $x = 0, l$). We simulated the model for natural condition corresponding to no flux boundary conditions:

$$\frac{\partial b}{\partial x}|_{x=0} = \frac{\partial b}{\partial x}|_{x=l} = 0. \tag{12}$$

Table S1: Physical parameters used in simulations shown in main Figure 7. The precise value of many parameters are not specified because they drop out of the non-dimensional model parameters, shown in Table S2, thus their values do not affect model predictions.

Parameter	Description	Value	Source / note
l	Length of leading edge	$40\,\mu$m	measured here
w	Width of leading edge	$1\,\mu$m	[S4]
v_0	Velocity of actin polymerization	$0.2\,\mu$m/ s	measured here
γ	Filament capping rate in low VASP	$1\,\mathrm{s}^{-1}$	[S8]
D	Diffusivity of cytosolic VASP	$0.2\,\mu\mathrm{m}^2/s$	estimated here
τ	Decay time of mature adhesions	30 s	[S4]
β_0	Branching rate (per length of leading edge)	$\mu\mathrm{m}^{-1}\,\mathrm{s}^{-1}$	not specified
β_1	Increase in branching rate by polymerization	$\mu\mathrm{m}^{-1}\,\mathrm{s}^{-1}$ per μm/ s	not specified
ν^+	Formation rate of nascent adhesions	s^{-1}per filament	not specified
ν^-	Decay rate of nascent adhesions	s^{-1}	not specified
μ	Maturation rate of nascent adhesions	s^{-1}	not specified
k_{cf}	VASP exchange	s^{-1}per filament	not specified
k_{fc}	VASP exchange	s^{-1}	not specified
k_{cm}	VASP exchange	s^{-1}per mature adhesion	not specified
k_{mc}	VASP exchange	s^{-1}	not specified
a_0	Amount of a_f that reduces capping by 50%	mol. per μm	not specified
d	Delivery rate of cytosolic VASP	mol. per μm/ s	not specified
Θ	Membrane tension	$\approx 100\,$pN/ μm	[S12, S16],
E	Membrane tension increase by polymerization	$\approx 10\,$pN/ μm	[S16]
f_{stall}	Polymerization force per filament	$\approx 1\,$pN/ filament	[S7, S14]

Those would arise, for example, under the assumption that left-facing barbed ends become stalled at the left corner, but maintain the ability to nucleate a branched (and therefore right-facing) barbed end. We also tried simply to keep the barbed end density at the ends equal to a small fixed value, $b(0) = b(l) = b_0$. In this case, the wave tends to initiate away from the leading edges end. We also tried changing the values of $m(x)$ at $x = 0$ and $x = l$, $m(0) = m(l) = m_0$, even though the equation for m does not require boundary conditions, corresponding to a fixed adhesion density at the ends. Similarly to fixing the barbed end density at the ends, most results remain unchanged; however, waves tend to initiate away from the leading edge corners, where they initiate in doublets that travel in opposite directions.

2 Model analysis and simplifications

Separation of timescales and non-dimensionalization

The predominant timescale is the rate of VASP removal by diffusion away from the leading edge, $t^\star = w^2/D \approx 5\,\mathrm{s}$. Compared to this, barbed-end dynamics are fast, with timescale $\epsilon\, t^\star$ where $\epsilon = D/w^2\gamma \approx 0.1$. We now identify dynamics that are slower than these timescales. Roughly speaking, each dynamic variable that has fast dynamics relative to the timescale of interest eliminates one of the above equations.

- VASP exchange between cytosol, barbed-ends and adhesions is fast relative to other dynamics.
- Nascent adhesion turnover is fast relative to other dynamics.

With those timescale separations, we choose the following scales for the dynamic variables, space and time:

$$b = \frac{\beta_0}{\gamma_0} B \qquad\qquad \approx (100\,\mu\text{m}^{-1})\ B \tag{13}$$

$$a = \frac{k_{bc}}{k_{cb}} \frac{\gamma_0}{\beta_0} A \tag{14}$$

$$m = \frac{k_{mc}}{k_{cm}} M \tag{15}$$

$$t = \frac{w^2}{D} T \qquad\qquad \approx (5\,\text{s})\ T \tag{16}$$

$$x = v_0 \frac{w^2}{D} X \qquad\qquad \approx (1\,\mu\text{m})\ X \tag{17}$$

This leads to the nondimensional system of three coupled differential equations,

$$\epsilon \frac{\partial B}{\partial T} = (1 + \eta_B V) - \frac{B}{1 + AB/(1 + M + KB)} + \epsilon^2 \frac{\partial}{\partial X} \left(\frac{1}{\Gamma} \frac{\partial B}{\partial X} \right) \tag{18}$$

$$\frac{\partial A}{\partial T} = d - \frac{(1 + \eta_A V + \eta_M M V) A}{1 + M + KB} \tag{19}$$

$$\frac{\partial M}{\partial T} = RB - (\theta + \eta_M V) M. \tag{20}$$

We define the nondimensional parameters (each related to a set of physical parameters) below. The nondimensional auxiliary variable

$$\Gamma = 1 + AB/(1 + M + KB) \tag{21}$$

is related to a spatially-varying diffusion process. The protrusion velocity is given by

$$V = (1 - (B_c/B)^8) \tag{22}$$

where the membrane tension Θ is transformed into a critical barbed-end density B_c. Following the assumptions about protrusion's effect on membrane tension,

$$B_c = \begin{cases} B_c^0 & \int V dX = 0 \\ B_c^0 (1 + E) & \int V dX > 0 \end{cases} \tag{23}$$

where $B_c^0 = \Theta_0 / f_{\text{stall}}$.

From the total local VASP concentration $A(x, t)$, we compute the portion in each compartment (cytosolic, mature adhesion and barbed-ends, respectively), as

$$A_c = \frac{1}{1 + M + KB}\ A \tag{24}$$

$$A_m = \frac{M}{1 + M + KB}\ A \tag{25}$$

$$A_b = \frac{KB}{1 + M + KB}\ A. \tag{26}$$

Table S2: Nondimensional parameters. Results use values shown unless otherwise noted.

Parameter	Definition	Description	Value
R	$\mu k_{cm}/k_{mc}$	Scaled maturation rate	0.2, varied
δ	dw^2/Da_0	Scaled VASP delivery rate	0.9, varied
ϵ	$\gamma w^2/D$	Ratio of actin dynamics timescale to VASP timescale	0.1
η_B	$\beta_1 v_0/\beta_0$	Increase in actin branching due to polymerization	1
η	$v_0 w/D$	Scaled adhesion advection rate	1
K	$\frac{\beta_0/\gamma_0}{(k_{bc}/k_{cb})}$	Scaled ratio of reaction constants of VASP-to-actin and VASP-to-adhesion	1
B_{crit}	$\Theta_0/f_{\text{stall}}\beta/\gamma$	Critical barbed end density allowing protrusion	4
E	$\Delta\Theta/\Theta_0$	Scaled increase in critical barbed end density due to protrusion	0.1

Parameters in the non-dimensional model

The nondimensional parameters in Eqs. 18-20 are:

$$\epsilon = \frac{1}{\gamma_0}\frac{D}{w^2} \qquad \approx 0.1 \tag{27}$$

$$\eta = \frac{v_0 w}{D} \qquad \approx 0.2 \tag{28}$$

$$\theta = \frac{w^2}{D\tau} \qquad \approx 0.05 \tag{29}$$

$$\eta_B = \beta_1 v_0/\beta_0 \qquad = 1 \text{ (assumed)} \tag{30}$$

$$K = \frac{\beta_0/\gamma_0}{(k_{bc}/k_{cb})} \qquad = 1 \text{ (assumed)} \tag{31}$$

$$R = \frac{w^2\nu^+(\beta_0/\gamma_0)}{D\nu^-(k_{mc}/k_{cm})}\cdot\mu \qquad \text{varied} \tag{32}$$

$$\delta = \frac{w^2(\beta_0/\gamma_0)}{D(k_{bc}/k_{cb})a_0}\cdot d \qquad \text{varied} \tag{33}$$

The parameters constrained by the data are ϵ, η and θ, as well as the base time scale w^2/D and length scale $v_0 w^2/D$. These parameters are derived from experimentally well-constrained values. Parameters δ and R are unknown, and so we explore variability in these parameters in a wide range. For the remaining two parameters, we set $\eta_B = K = 1$. The meaning of parameter η_B is the ratio of the speed-dependent to speed-independent parts of the branching rate. The analysis shows that if this ratio is much less than 1, then the positive feedback between protrusion and branching rate is weak and the waves do not emerge. This is in agreement with the data from Arp2/3 inhibition experiment. If this parameter is much great than 1, the models conclusions do not change. The meaning of parameter $K = 1$ is the partitioning of VASP between the barbed ends and mature adhesions. VASP images in this study, as well as in [S15], suggest that this partitioning is not too far from equal, hence the assumption that $K = 1$.

3 Numerical simulation of model

Traveling wave train at high adhesion and intermediate VASP

For $\delta = 0.9, R = 0.2$, numerical simulation of Eqs. 18-20 result in a sequence of traveling waves. This solution evolves from every initial condition we tried, including uniformly stalled, uniformly protruding, random and gradients, and they persist for the duration of long simulations to $> 10^4$ seconds. A profile of concentrations in the wave, at an instant in time, is shown in Fig. S8.

Properties of waves predicted by the model

The following properties occur over a wide range of model parameters:

- Lateral wave velocity is equal to actin polymerization velocity.
- Typically, traveling waves start at edges or location of previous traveling wave. Waves tend to initiate at the corners ($x = 0$ and $x = l$). Occasionally, a wave initiates at the edge away from the corners, in which case the wave initiates as a doublet of waves traveling in opposite directions, and the nucleation site migrates slowly between subsequent waves (Fig. 6Biii of the main text).
- After an initial transient at the beginning of simulation, the next traveling wave (or doublet of traveling waves) begins immediately after the previous wave dies out.
- Locally, total VASP concentration exhibits a traveling wave with phase slightly ahead of actin protrusion traveling wave.
- Locally, adhesion density exhibits a traveling wave that is out of phase with the actin/protrusion traveling wave.

The following properties are satisfied for our choice of $\delta = 0.9$ and $R = 0.2$:

- Excited time period is roughly half the refractory time period, and the excited protrusion is roughly one third the length of the leading edge.
- The amplitude of actin oscillations is $\sim 70\%$ of its minimal value.
- The amplitude of adhesion oscillations is $\sim\ 50\%$ of its minimal value.

Quantitative explanation of waving

From a physical point of view, the emergence of waves can be understood by examining the time series of local concentrations at a point along the leading edge, shown in Fig. S8. When this region is stalled, VASP accumulates as it is delivered to barbed ends faster than it diffuses away through the cytosol. The increasing VASP concentration brings with it an increase in barbed-end density, through anti-capping activity, until there are enough barbed ends to cause protrusion. At this point, VASP delivery is insufficient to dominate over VASP removal (via the relative rearward motion of mature adhesion and, depending on which model variant, the relative rearward motion of the cytosol), and local VASP concentration decreases. Without sufficient VASP to prevent capping, the barbed-end density reduces until the leading edge stalls, and the cycle repeats. As the traveling wave is lost at one of the boundaries, membrane tension is slightly reduced. This initiates the following traveling wave in the sequence.

From the point of view of dynamical systems, the emergence of a sequence of traveling waves can be understood qualitatively as follows. The underlying system of ordinary differential equations (ODEs), i.e., Eqs. 18-20 without the diffusion term, demonstrates several classes of solution, depending on the parameters: a stable steady state with $V = 0$, a stable steady state with $V \approx 1$, two steady states corresponding to bistability, and oscillations [S22]. For solutions with the $V = 0$ steady state, the system is excitable [S6], and a sufficient perturbation results in a large excursion in $B(t), A(t)$ and $M(t)$ before returning to the stable steady state. Among the parameters controlling the dynamics is B_c. The sequence of traveling wave occurs when $B_c = B_c^0$ is oscillatory, while $B_c = B_c^0(1 + E)$ is excitable. Thus, when $V = 0$ for all X, the system varies until protrusion begins for some X. At this point, B_c increases, the system becomes excitable, and the protrusion propagates as an excitable wave [S6] via the lateral diffusion term in Eq. 18.

Phase diagram for varying model parameters

As mentioned, the solutions to Eqs. 18-20 depend on parameters, including δ and R. We ran simulations for 221 parameter sets with $\delta \in [0, 0.2]$ and $R \in [0.6, 1.0]$ and summarize the results in Fig. 6 of the main text and Fig. S9.

For these parameters, we observe leading edges that are stalled, smooth motile or waving, separated by predicted transition lines shown as dashed lines in Fig. S9A. Some sample kymographs of these simulations are shown in Fig. 6B of the main text and summarized here.

(i) Sequence of traveling waves as described in the previous section.

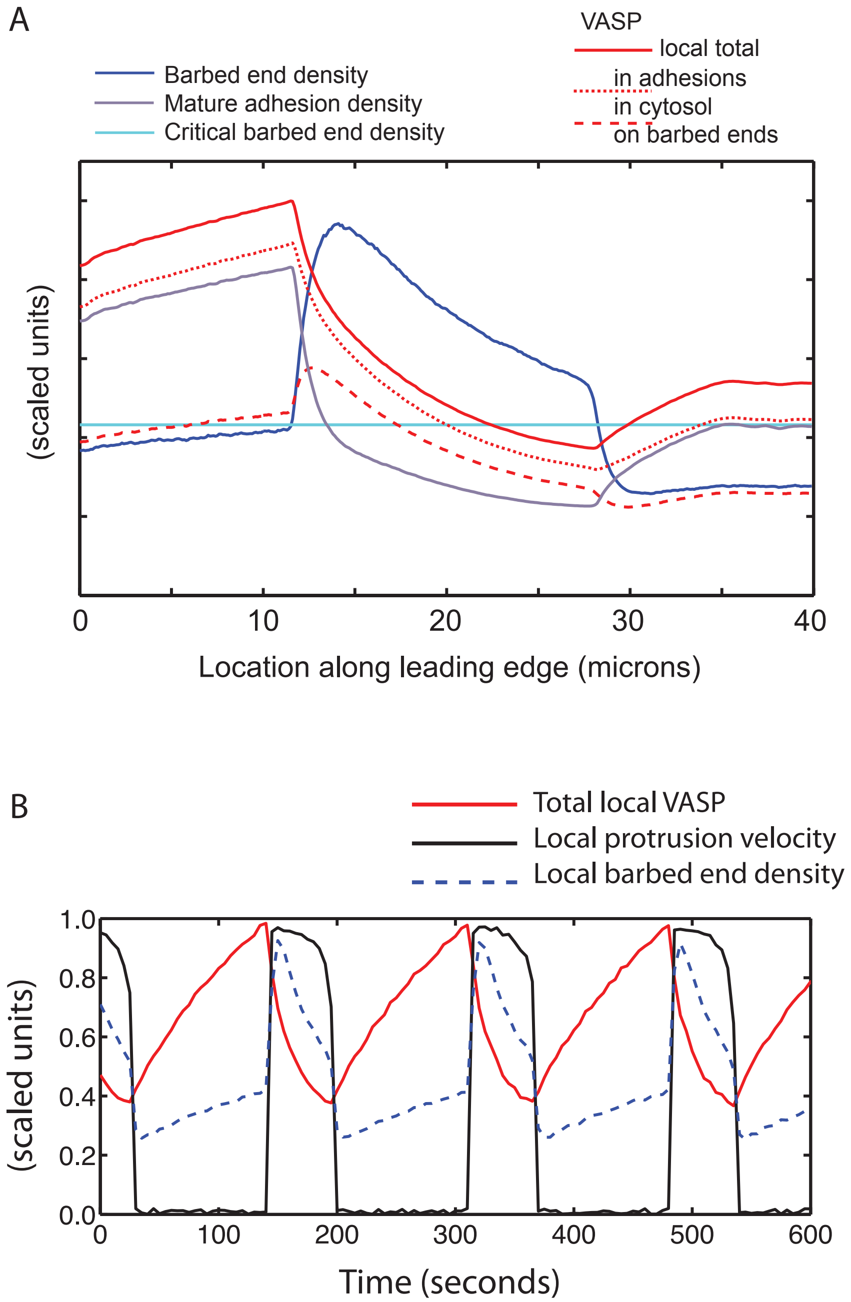

Fig. S8: Simulated traveling waves at high adhesion and intermediate VASP concentrations. (A) Profile of concentrations along the leading edge at a particular time. The wave moves to the left. Cyan line indicates the barbed-end density threshold above which protrusion occurs. Total VASP is shown by the solid red curve, and the area below this curve is split into three sub-populations. (B) Time series of local concentrations at a particular location along the leading edge.

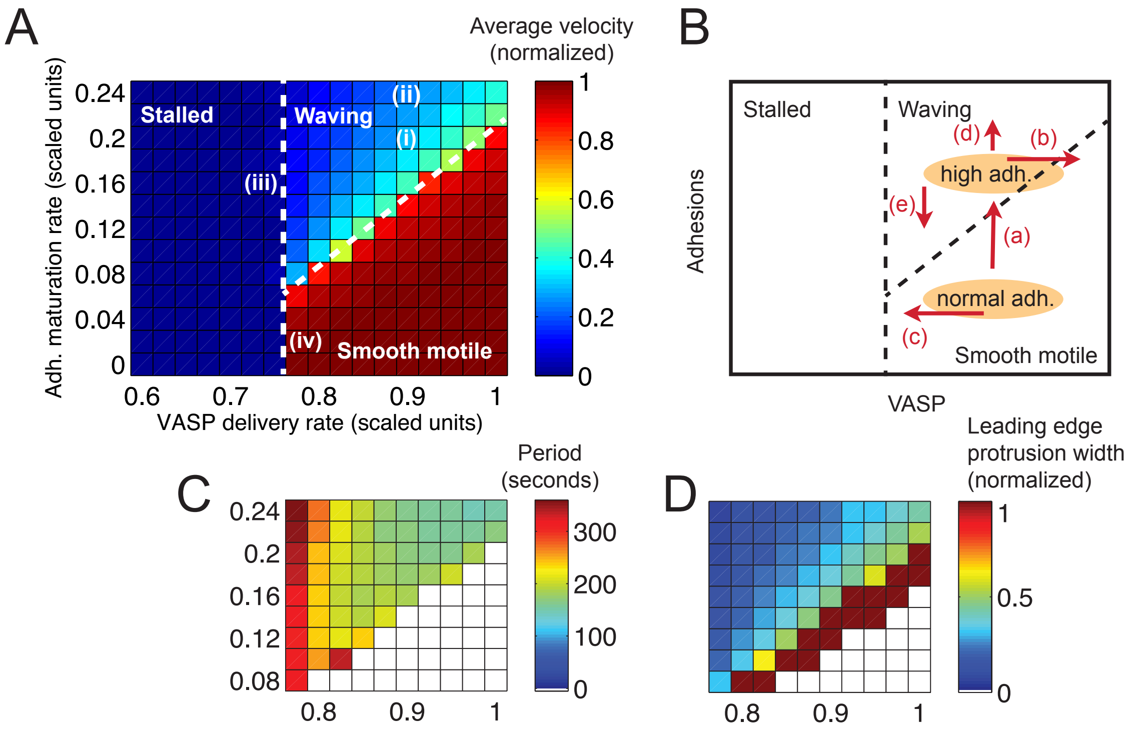

Fig. S9: Phase diagram showing leading edge behavior as a function of two model parameters, VASP delivery rate δ and adhesion maturation rate R. (A) Average velocity. Dashed lines show predicted transitions between stalled, waving, and smooth motile leading edges. Roman numerals (i)-(iv) correspond to kymographs in Fig. 6 of the main text. (B) Predictions for molecular perturbation experiments. Shaded regions indicate intrinsic population variability. (a) Increasing adhesion maturation by increasing substrate adhesion leads to waving. (b) Overexpression of VASP at high adhesion reduces the fraction of cells that wave. (c) Depletion of VASP at low adhesion does not introduce waves, and may stall some cells. (d) Promoting adhesions, for example with FAK, results in thinner waves as shown in Fig. 6ii. (e) Reducing adhesion maturation with blebbistatin reduces the fraction of cells that wave. (C-D) For the region of parameter space exhibiting waves, the wave period in seconds (C), and the duty ratio (D), defined as the fraction of the period for which there is protrusion. Hotter colors represent more thicker waves.

(ii) Traveling waves with various lateral widths. Since the propagation velocity is approximately constant v_0, the width of the wave is ρl where $\rho = T_{\mathrm{exc}}/T$ is the duty ratio, the ratio of time a region of leading edge is protruding relative to the period of oscillation, T. The model produces all duty ratios $\rho \in [0, 1]$ for different parameters, shown in Fig. S9D.

(iii) Stalled leading edges which support wave pulses. By starting with an initial condition in which a location along the leading edge has $B(X) > B_c^0$, a single wave pulse travels along the leading edge and then vanishes.

(iv) Motile leading edges which support wave fronts. By starting with an initial condition with $V = 0$ everywhere, protrusion begins at a location and travels along the leading edge until protrusion is everywhere. These states correspond to bistability in the ODEs discussed above.

Model predictions for molecular perturbation experiments

As described in the main text, keratocytes were perturbed with pharmacological agents and exposed to surfaces with different adhesion strengths. These perturbations correspond to changes in parameters in the mathematical model. Here we describe changes in leading edge behavior predicted by these perturbation experiments. Each prediction agrees with the experimental results.

(a) Increasing adhesion maturation by increasing substrate adhesion leads to waving.

(b) Overexpression of VASP at high adhesion reduces the fraction of cells that wave.

(c) Depletion of VASP at low adhesion does not introduce waves, and may stall some cells.

(d) Promoting adhesions with focal adhesion kinase (FAK) results in thinner waves as shown in Fig. 6Bii of the main text.

(e) Reducing adhesion maturation with blebbistatin reduces the fraction of cells that wave.

These molecular perturbations are summarized by the arrows in Fig. S9B.

Other leading edge behavior occurring in the model

Noisy leading edge

As mentioned above, we include a noise term in Eq. 1 with autocorrelation $\langle \xi(t)\xi(t-t')\rangle = \xi_0^2\delta(t-t')$. In the nondimension model, the transformed noise term is Ξ_T with autocorrelation $\langle \Xi(T)\Xi(T-T')\rangle = \Xi_0^2\delta(T-T')$ where $\Xi_0 = \xi_0\gamma_0 D/(\beta_0 w^2)$.

At high levels of noise, $\Xi_0 = 10^{-1}$, for parameters $\delta = 0.7, R = 0.2$, simulations result in a noisy leading edge where small, short-lived traveling waves are continuously forming. Traveling waves have a characteristic propagation velocity of $\approx v_0 = 0.2\,\mu\text{m}/\,\text{s}$. An example is shown in Fig. S10A. These noisy simulations are reminiscent of rough leading edges observed experimentally (see Fig. 1F in the Main Text).

Low-amplitude uniform oscillations

For intermediate VASP and high adhesion maturation ($\delta = 0.9, R = 0.2$), when the nondimensional parameter ϵ is increased to $\epsilon = 15$, the leading edge undergoes synchronized oscillations of protrusion, in which the velocity oscillates with a nonzero minimum (in contrast to large-amplitude oscillations discussed below). These are shown in Fig. S10B. The amplitude of these waves gradually decays, approaching to a constant velocity. The increase in $\epsilon = w^2/D/\gamma$ can be interpreted as a reduced turnover rate in the actin network. The resultant low-amplitude oscillations may correspond to experimental observations (see Fig. 1J in the Main Text).

4 Model variants testing alternative hypotheses

- **VASP as an actin polymerization promoter.** An alternative suggested role of VASP is in promoting actin polymerization [S10]. We test this hypothesis by replacing Eq. 6 with

  $$v = \begin{cases} v_0(1 + a_b/a_1)\left(1 - (\Theta/(f_{\text{stall}}b))^8\right) & b > \Theta/f_{\text{stall}} \\ 0 & b < \Theta/f_{\text{stall}} \end{cases} \tag{34}$$

  where a_1 is a parameter describing the amount of VASP that doubles the actin polymerization rate. In the arrow diagram in Fig. 5 of the main text, this can be interpreted as an arrow directly from VASP to protrusion.

  Our simulations in which VASP has polymerization-promoting activity, but no anti-capping activity, do not result in waves. The underlying ODE system does not have an oscillatory regime or an excitable regime. Simulations with both anti-capping and polymerization-promoting activities are qualitatively similar to anti-capping alone.

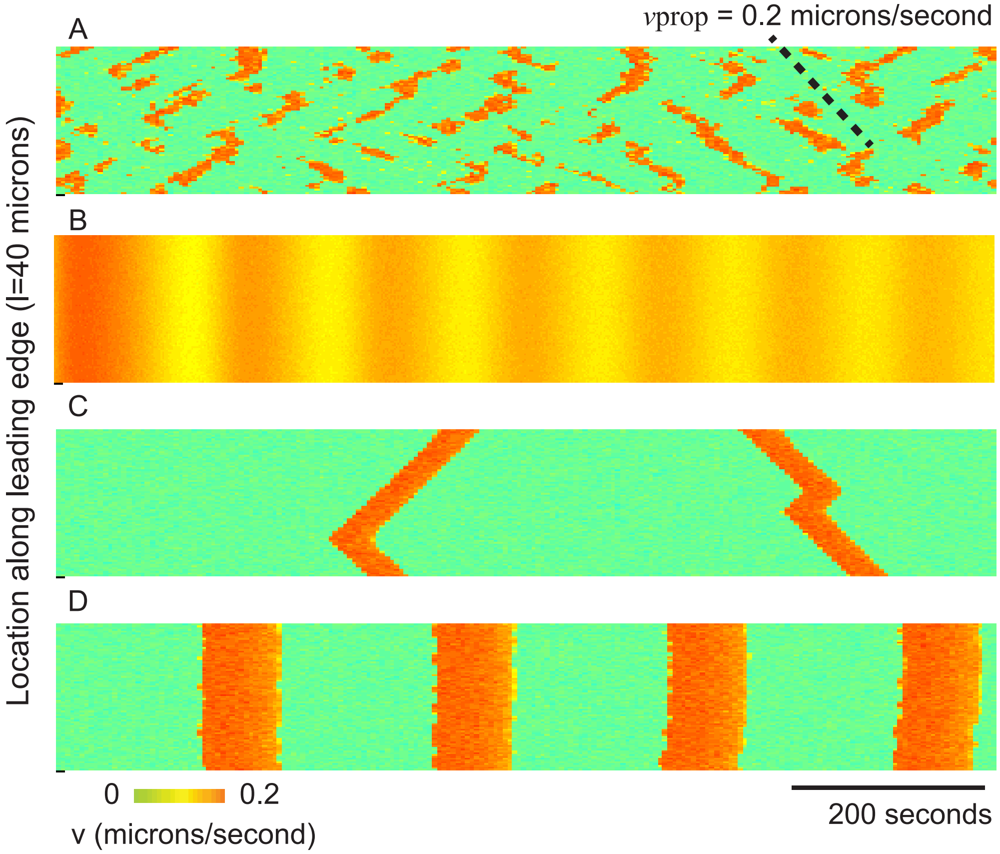

Fig. S10: Additional simulated leading edge behaviors. (A) Noisy leading edge with continuous, small traveling waves. The characteristic velocity of the traveling waves (slope of dashed line) is v0. (B) Low-amplitude oscillations of motile cells. (C,D) Model with constant membrane tension and small noise magnitude (C) or intrinsic oscillations (D).

- **Different assumption about relative cytosolic flow.** Recent evidence [S13] suggests that in steady-state, cytosol flows toward the leading edge at low velocity, however the relevance of this result to transient protrusion reported here is unclear. We explored the possibility that cytosolic VASP remains with the leading edge and found the results are insensitive to this assumption, although they require more mature adhesions, achieved in the model via a higher maturation rate μ (nondimensonal R) by a factor of three.

- **Constant membrane tension.** The model assumption with least experimental support is our assumption that membrane tension is slightly reduced in the absence of polymerization. We ran simulations without this assumption by setting $E = 0$. Two regimes of parameter space provided opportunity for traveling waves. For parameters where the underlying ODE is oscillatory, the leading edge exhibited synchronized oscillations between stalled and protruding. A kymograph is shown in Fig. S10D. Such behavior is not observed in keratocytes.

  Alternatively, in parameter regimes where the underlying ODE is excitable, a sequence of traveling waves is observed when a noise term is added to the equations as described in the previous section. For low levels of noise ($\Xi_0 = 10^{-3}$ in the previous section), this produces rare, spatially-uncoupled traveling waves shown in Fig. S10C. For increasing noise, we observe the rough leading edge described in the previous section.

- **Waves laterally driven by diffusing regulators.** Traveling waves of actin observed in other contexts and cell types have been hypothesized to travel via the diffusion of an actin regulator. These include hem1 in neutrophils [S24], membrane-bound proteins [S5], Rac [S27] and generic diffusible activator [S20]. In these cases, the traveling wave is predicted to have a propagation velocity $v_{prop} \approx \sqrt{2D\tau}$ where D is the diffusion coefficient of the actin regulator and τ is the characteristic timescale of its dynamics near the equilibrium state. We did not simulate such a mechanism, but note that it would not explain the strong correlation between propagation velocity and protrusion velocity observed experimentally.

5 Dynamics away from the leading edge

The above modeling considers the dynamics in a thin strip at the leading edge. For this reason, the model necessarily assumes phenomenological dynamics for delivery and removal of leading-edge molecular participants like VASP. In this section, we extend the model to a wide (rectangular, with dimensions similar to that of the whole keratocyte lamellipodim, which actually is very close to rectangle in shape, in the case of steady motility) strip near the leading edge. We can therefore study the influence of specific mechanisms of, e.g., VASP delivery.

Model description

This two-dimensional model is shown schematically in Fig. S11. Let y denote distance from the leading edge. Uncapped barbed ends are assumed to be primarily at the leading edge, therefore $B(x,t), A_b(x,t)$ and $V(x,t)$ are only defined at $y = 0$. The non-dimensional equations for variables $B(x,t), A_b(x,t)$ now have the form:

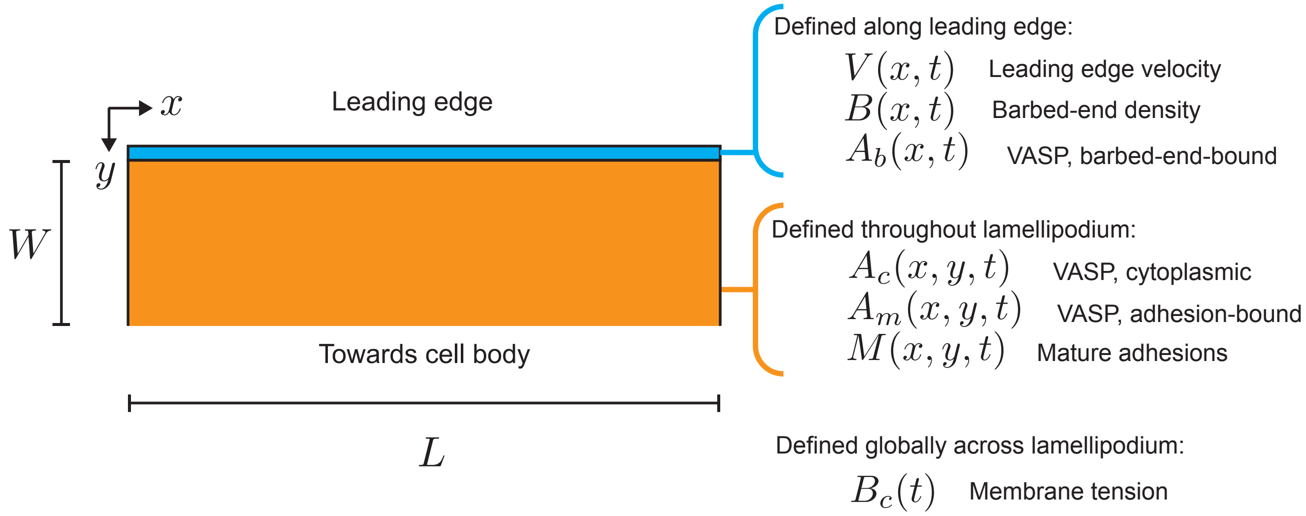

Fig. S11: Model geometry including dynamics away from the leading edge. The lamellipodium is approximated as a rectangle with leading edge length L, and width away from the leading edge W.

$$\epsilon \frac{\partial B}{\partial T} = (1 + \eta_B V) - \frac{B}{1 + A_b(X,0,T)} + \epsilon^2 \frac{\partial}{\partial X}\left(\frac{1}{\Gamma}\frac{\partial B}{\partial X}\right) \tag{35}$$

$$\frac{\partial A_b}{\partial T} = +k_2 \left(BA_c - A_b\right) \tag{36}$$

The equation for $V(x,t)$ remains unchanged. The remaining variables are defined throughout the lamellipodium and are therefore defined for all x and y in the domain.

VASP in cytoplasm. In this extension of the model, it is necessary to separate VASP states since these may have different transport kinetics. Cytosolic VASP undergoes exchange with mature adhesions and diffuses, leading to the non-dimensional PDE:

$$\frac{\partial A_c}{\partial T} = +k_3\left(A_m - KMA_c\right) + D_A\left(\frac{\partial^2 A_c}{\partial Y^2} + \frac{\partial^2 A_c}{\partial X^2}\right). \tag{37}$$

At the leading edge, cytosolic VASP exchanges with the leading edge,

$$D\frac{\partial A_c}{\partial Y} = +k_2\left(BA_c - A_b\right) \qquad \text{at} \qquad Y = 0, \tag{38}$$

while the cell body at the read of the lamellipodium provides a constant reservoir,

$$A_c = \delta \qquad \text{at} \qquad Y = W. \tag{39}$$

Mature adhesions. Mature adhesions advect backwards, and carry their VASP subpopulation with them:

$$\frac{\partial M}{\partial t} = -V(X)\frac{\partial M}{\partial Y}. \tag{40}$$

Mature adhesions are created from nascent adhesions, which are proportional to barbed ends (as in the 1D model, nascent adhesions are assumed to be proportional to B), so:

$$VM = RB \qquad \text{at} \qquad Y = 0. \tag{41}$$

VASP bound to adhesions. The subpopulation of VASP in mature adhesions exchanges with the cytoplasm and advects rearward, in tandem with the mature adhesions themselves:

$$\frac{\partial A_m}{\partial t} = -k_3\left(A_m - KMA_c\right) - V(X)\frac{\partial A_m}{\partial Y}, \tag{42}$$

with no-flux boundary condition at the leading edge:

$$A_m = 0 \qquad \text{at} \qquad Y = 0. \tag{43}$$

Results of simulation of 2D model

We have performed simulations of the above model for a limited range of parameters. The same behavior at the leading edge is exhibited as for the 1-d approximation model. Specifically, we observe a train of traveling waves, see Fig. S12, for parameters $R = 0.14, \delta = 5, E = 0.2, \eta_M = 1, K = 1, k_2 = 1, k_3 = 10, B_c^0 = 3.6, D_A = 1$. The behavior changes upon changing parameters, like in the 1-dimensional approximation model. For example, a stalled (non-motile) leading edge that supports individual traveling pulses of protrusion upon perturbations is also exhibited, as shown in Fig. S13, for parameters $R = 0.14, \delta = 2, E = 0.1, \eta_M = 1, K = 1, k_2 = 10, k_3 = 10, B_c^0 = 3.6, D_A = 1$.

The 2-d model that includes dynamics away from the leading edge, confirms the general results provided by our simpler 1-dimensional model. In addition, it elucidates a specific question about VASP delivery: We find that diffusion alone is sufficient to deliver VASP to the leading edge at a rate consistent with its consumption by the growing barbed ends. Interestingly, at the same time this diffusion is not too great and does not abolish the spatial heterogeneity along the leading edge, in agreement with the experimental data. Finally, note that the 2-d VASP diffusion translates into the delivery to the edge with the effective speed of the order of the diffusion coefficient divided by the effective length on which VASP is partially depleted by "consumption" at the edge. For realistic parameters, the effective delivery speed is at least a few-fold greater than the protrusion speed, and so the latter can be neglected.

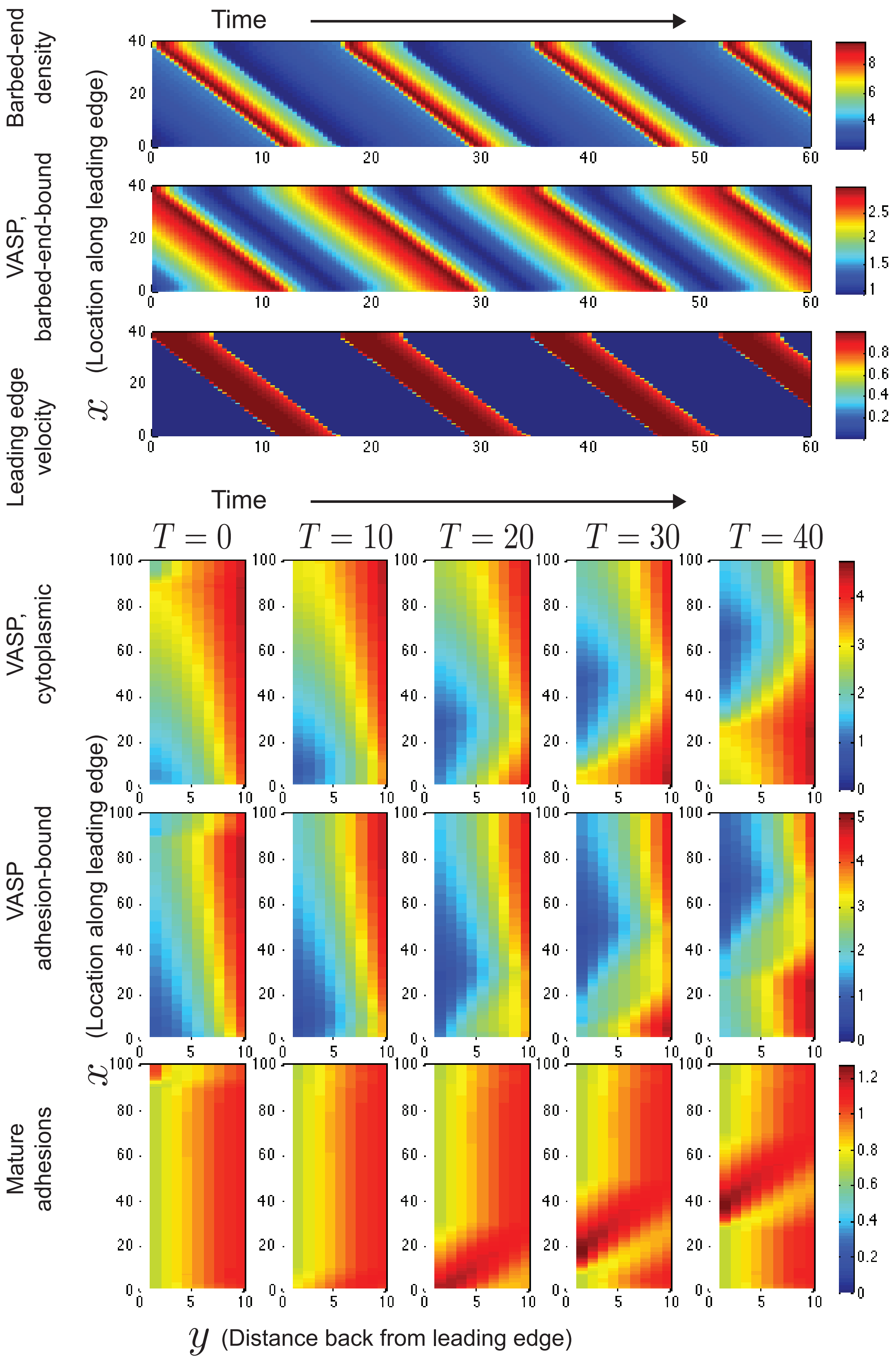

Fig. S12: Train of traveling waves of protrusion in the full-lamellipodium (2-dimensional) model.

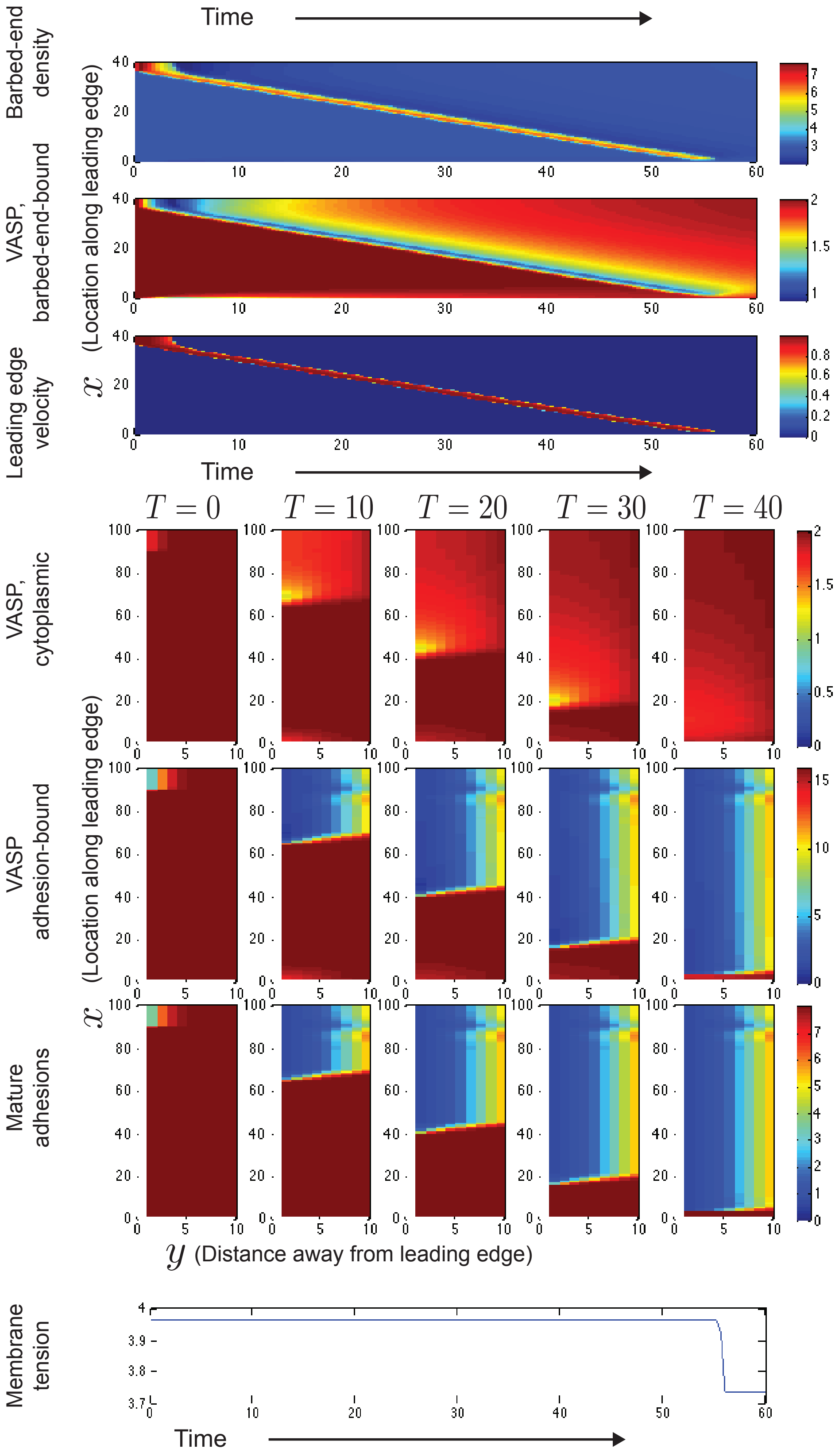

Fig. S13: Example of a single excitation wave of protrusion in the full-lamellipodium (2-dimensional) model.

6 Model modification in the case of a dynamic leading edge

One of the simplifications of the above modeling is the assumption of a steady leading edge shape, specifically, that its shape deformations are small. Obviously, such approximation is rather drastic for the waving cells: one can glean from the time-lapse microscopy that the shape of the leading edge changes significantly in time. For the densities of the barbed ends, mature adhesions and VASP, these leading edge deformations lead to two effects: First, if the leading edge contour expands / shrinks locally, then all densities have to respectively decrease / increase locally as well. Second, due to the lateral flow of two oppositely oriented actin branches subpopulations at the leading edge, deformations of the edge lead to effective drift of the barbed end density. Here, we derive the model modification in the case of the leading edge as a free boundary and describe numerical results that demonstrate that such model extension does not change the main conclusions of this study.

Model description

We approximate the dynamic shape of the leading edge as follows: we assume that the leading edge is still parametrized by $0 < x < l$, where l is the total length of the edge, however, we do not treat the edge as a static arc anymore, but rather describe its shape with the function $f(x, t)$ so that $y = f(x)$ is the set of points constituting the leading edge curve at time t. Thus, x-coordinates of the leading edge ends do not shift in time (equivalent to the assumption that the sides of the cell move along straight parallel lines), but the shape of the edge between the corners is dynamic. Furthermore, we assume that the leading edge shape does not deviate from the straight line too much, so that the local curvature of the edge $1/r$ can be described by the formula $\partial^2 f/\partial x^2$. In the case of large edge deformations, all formulas and calculations become prohibitively complex, and in any case, other model approximations become dubious, so the full 2D free boundary problem would have to be solved, which at this time poses a paramount challenge, besides bringing little insight.

We derived equations for the reaction-drift-diffusion processes on the moving boundary in [S17]. If $\phi(s, t)$ is a density on the cell boundary, where s is an arc coordinate along the boundary, then the equation on the steady boundary,

$$\frac{\partial \phi}{\partial t} = T + R, \tag{44}$$

where T and R are the transport and reaction terms, respectively, change to

$$\frac{\partial \phi}{\partial t} = T + R - \frac{V(s)}{r(s)}\phi. \tag{45}$$

Here V is the rate of locally normal protrusion and r is the local edge radius of curvature. In the approximation of small edge deformations, $V(s)$ is the same protrusion velocity we used in the model above, and coordinate s can be approximated by x. The additional term has simple meaning: if $r > 0$, then when the curving out edge protrudes, the local edge length increases leading to local depletion of the density. In [S17], we demonstrated that in the case of arbitrary deformations, there is another, nonlocal, term that has to be added to the density equations, but in the limit of small deformations that term is negligible.

Second, we demonstrated in [S15] that there is an additional drift term for the barbed end density at the deforming leading edge. This term originates from the phenomenon of the lateral flow: barbed ends of the filaments branching to the right/left drift to the right/left, respectively, along the edge as they grow. In [S15] we discuss experimental evidence that the predominant orientation of the barbed ends is global, $\pm 35^o$, independent of the local orientation of the leading edge. In this case, for example, if $\partial f/\partial x > 0$, then the barbed ends of the filaments branching to the right would slide to the right faster, than the barbed ends of the filaments branching to the left slide to the left. In [S15], we demonstrated that this effect leads to the additional drift term

$$-(1/\cot(35^o))\frac{\partial}{\partial x}\left(v\frac{\partial f}{\partial x}b\right). \tag{46}$$

Finally, we need one additional equation for computing the leading edge shape, which is the kinetic equation $\partial f/\partial t = v(x)$. Clearly, we could add the centripetal myosin-driven flow to this equation, and/or write it in the framework of the moving cell center-of-mass, but this only shifts the edge in space as a whole and does not change anything relevant to the model behavior. We also have to add the second term to the right hand side of this equation, which describes the correction of the protrusion rate due to the local membrane curvature, $\partial^2 f/\partial x^2$: if a protrusive lobe develops, $\partial^2 f/\partial x^2 < 0$, there is a restoring force trying to flatten the membrane, while if there is a local indentation in the leading edge (part of the leading edge lags behind, $\partial^2 f/\partial x^2 > 0$), then membrane tension at the sides restores flatness helping the protrusion. Such term was derived and discussed at length in [S9, S15]. Because the membrane resistance is proportional to the Gaussian curvature at the leading edge [S9], the main component of which is the high curvature in the dorsal-ventral direction, the nondimensional proportionality coefficient, $\tilde{\epsilon}$, for this additional term in the equation for f responsible for the lateral bending of the leading edge is small, on the order of 0.1 [S15].

After the non-dimensionalization, which uses the same scales as in the basic model , the non-dimensional model (Eq. 18 -Eq. 20) on the moving boundary has the form:

$$\epsilon \frac{\partial B}{\partial T} = (1+\eta_B V) - \frac{B}{1+AB/(1+M+KB)} + \epsilon^2 \frac{\partial}{\partial X}\left(\frac{1}{\Gamma}\frac{\partial B}{\partial X}\right) + \epsilon \frac{\partial^2 F}{\partial X^2} B - \epsilon \frac{\partial}{\partial X}\left(V \frac{\partial F}{\partial X} B\right) \tag{47}$$

$$\frac{\partial A}{\partial T} = d - \frac{(1+\eta_A V + \eta_M M V)A}{1+M+KB} + \epsilon \frac{\partial^2 F}{\partial X^2} A \tag{48}$$

$$\frac{\partial M}{\partial T} = RB - (\theta + \eta_M V)M + \epsilon \frac{\partial^2 F}{\partial X^2} M \tag{49}$$

$$\frac{\partial F}{\partial T} = V + \tilde{\epsilon} \frac{\partial^2 F}{\partial X^2}. \tag{50}$$

The other equations of the model, as well as the boundary conditions, are unchanged.

Results of simulation with leading edge shape corrections

We have performed simulations of the above system of equations for a limited range of parameters. A comparison between predictions of the models with and without correction terms is shown in Fig. S14. Generally, we find that the correction terms do not lead to large changes in the behavior of the system. The traveling wave pulses become thinner and more frequent, but this effect can be compensated by a slight changes in parameters.

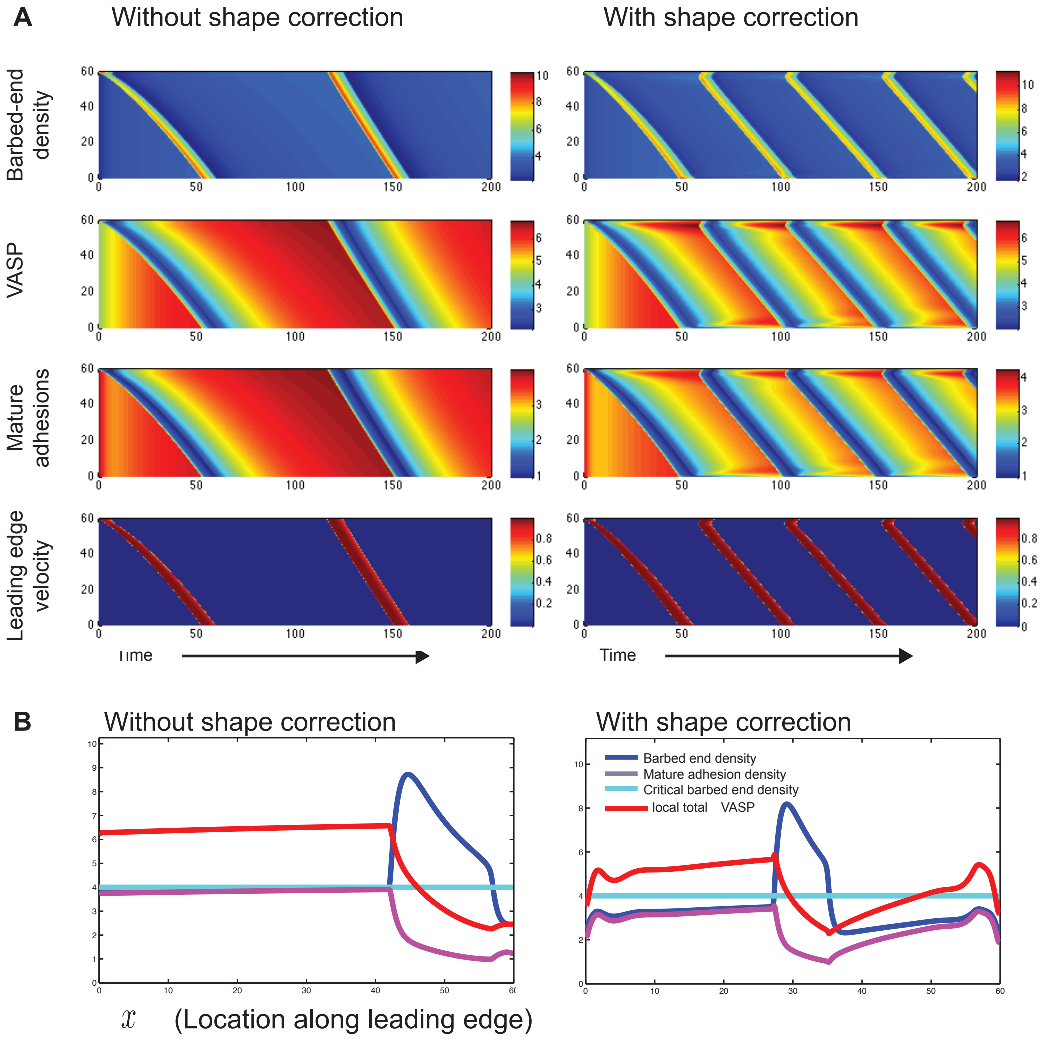

Fig. S14: Kymographs (A) and an instantaneous profile of local densities (B) for the model with dynamic leading edge shape (right column). The "correction terms" introduced to account for leading edge deformation do not have a strong qualitative effect compared to the model without these correction terms (left column). All parameters identical for both simulations: $R = 0.2, \delta = 0.75$, and all other parameters as in Table S2.

Supplemental References

S1. Barnhart, E.L., Allen, G.M., Julicher, F., and Theriot, J.A. (2011). Bipedal locomotion in crawling cells. Biophys. J., *98*(6):933–942.

S2. Bear, J.E., and Gertler, F.B. (2009). Ena/VASP: towards resolving a pointed controversy at the barbed end. J. Cell Sci., *122*(12):1947–1953.

S3. Carlsson, A.E. (2003). Growth velocities of branched actin networks. Biophys. J., *84*(5):2907–2918.

S4. Choi, C.K., Vicente-Manzanares, M., Zareno, J., Whitmore, L.A., Mogilner, A., and Horwitz, A.R. (2008). Actin and -actinin orchestrate the assembly and maturation of nascent adhesions in a myosin ii motor-independent manner. Nat. Cell. Biol., *10*(9):1039–1050.

S5. Döbereiner, H.-G., Dubin-Thaler, B.J., Hofman, J.M., Xenias, H.S., Sims, T.N., Giannone, G., Dustin, M.L., Wiggins, C.H., and Sheetz, M.P. (2006). Lateral membrane waves constitute a universal dynamic pattern of motile cells. Phys. Rev. Lett., *97*(3):038102.

S6. L Edelstein-Keshet (1988). Mathematical models in biology (SIAM).

S7. Footer, M.J., Kerssemakers, J.W.J., Theriot, J.A., and Dogterom, M. (2006). Direct measurement of force generation by actin filament polymerization using an optical trap. Proc. Natl. Acad. Sci., *104*(7) 2181–2186.

S8. Grimm, H.P., Verkhovsky, A.B., Mogilner, A., and Meister, J.J. (2003). Analysis of actin dynamics at the leading edge of crawling cells: implications for the shape of keratocyte lamellipodia. Euro. Biophys. J., *32*(6):563–577.

S9. Gov, N.S., and Gopinathan, A. (2006). Dynamics of membranes driven by actin polymerization. Biophys. J., *90*:454–469.

S10. Hansen, S.D., and Mullins, R.D. (2010). Vasp is a processive actin polymerase that requires monomeric actin for barbed end association. J. Cell. Biol., *191*(3):571–584.

S11. Howard, J. (2001). Mechanics of Motor Proteins and the Cytoskeleton (Sinauer).

S12. Keren, K., Pincus, Z., Allen, G.M., Barnhart, E.L., Marriott, G., Mogilner, A., and Theriot, J.A. (2008). Mechanism of shape determination in motile cells. Nature, *453*(7194):475–480.

S13. Keren, K., Yam, P.T., Kinkhabwala, A., Mogilner, A., and Theriot, J.A. (2009). Intracellular fluid flow in rapidly moving cells. Nat. Cell. Biol., *11*(10):1219–24.

S14. Kovar, D.R. and Pollard, T.D. (2004). Insertional assembly of actin filament barbed ends in association with formins produces piconewton forces. Proc. Natl. Acad. Sci., *101*(41):14725–14730.

S15. Lacayo, C.I., Pincus, Z., Vanduijn, M.M., Wilson, C.A., Fletcher, D.A., Gertler, F.B., Mogilner, A., and Theriot, J.A. (2007). Emergence of large-scale cell morphology and movement from local actin filament growth dynamics. PLoS Biol., *5*(9):e233.

S16. Lieber, A.D., Yehudai-Resheff, S., Barnhart, E.L., Theriot, J.A., and Keren, K. (2013). Membrane Tension in Rapidly Moving Cells Is Determined by Cytoskeletal Forces. Curr. Biol., *23*(15):1409–1417.

S17. Lomakin, A., Lee, K.-C., Han, S.J., Bui, D.A., Davidson, M., Mogilner, A. and Danuser, G. (2015) Competition for actin between two distinct F-actin networks defines a bistable switch for cell polarization. Nat. Cell. Biol., *17*(11):1435–1445.

S18. Mogilner, A. and Oster, G. (1996). Cell motility driven by actin polymerization. Biophys. J., *71*(6): 3030–3045.

S19. Pollard, T.D. and Borisy, G.G. (2003). Cellular motility driven by assembly and disassembly of actin filaments. Cell, *112*(4):453–65.

S20. Ryan, G. and Vavylonis, D. (2012). Excitable actin dynamics in lamellipodial protrusion and retraction. Biophys. J. *102*, 1493-1502.

S21. Seifert, U. and Langer. S. (1994). Hydrodynamics of membranes: the bilayer aspect and adhesion. Biophys. Chem., 1–10.

S22. Strogatz, S.H. (1994). Nonlinear Dynamics and Chaos (Westview Press).

S23. van Kampen, N.G. (2007). Stochastic Processes in Physics and Chemistry (North Holland).

S24. Weiner, O.D., Marganski, W.A., Wu, L.F., Altschuler, S.J., and Kirschner, M.W. (2007). An actin-based wave generator organizes cell motility. PLoS Biol., *5*(9):e221.

S25. Wilson, C.A., Tsuchida, M.A., Allen, G.M., Barnhart, E.L., Applegate, K.T., Yam, P.T., Ji, L., Keren, K., Danuser, G., and Theriot, J.A. (2010). Myosin II contributes to cell-scale actin network treadmilling through network disassembly. Nature, *465*(7296):373–377.

S26. Yeung, A., and Evans, E. (1995). Unexpected dynamics in shape fluctuations of bilayer vesicles. Journal de Physique II, *5*(10):1501–1523.

S27. Zeng, Y., Lai, T., Koh, C.G., Leduc, P.R., and Chiam, K.-H. (2011). Investigating circular dorsal ruffles through varying substrate stiffness and mathematical modeling. Biophys. J., *101*(9):2122–30.

axis of the juvenile but not the larva in a maximally indirect developing invertebrate, Micrura alaskensis (Nemertea). BMC Biol. *13*, 23.

16. Hiebert, L.S., and Maslakova, S.A. (2015). Expression of *Hox, Cdx*, and *Six3/6* genes in the hoplonemertean *Pantinonemertes californiensis* offers insight into the evolution of maximally indirect development in the phylum Nemertea. Evodevo *6*, 26.
17. Raff, R.A. (2008). Origins of the other metazoan body plans: the evolution of larval forms. Philos. Trans. R. Soc. Lond. B. Biol. Sci. *363*, 1473–1479.
18. Page, L.R. (2009). Molluscan larvae: Pelagic juveniles or slowly metamorphosing larvae? Biol. Bull. *216*, 216–225.
19. Sly, B.J., Snoke, M.S., and Raff, R.A. (2003). Who came first-larvae or adults? origins of bilaterian metazoan larvae. Int. J. Dev. Biol. *47*, 623–632.
20. Morgan, T.H. (1894). The development of balanoglossus. J. Morphol. *9*, 1–86.

Cell Migration: Making the Waves

Jan Müller and Michael Sixt*
Institute of Science and Technology Austria (IST Austria), am Campus 1, 3400 Klosterneuburg, Austria
*Correspondence: sixt@ist.ac.at
http://dx.doi.org/10.1016/j.cub.2016.11.035

Coordinated changes of cell shape are often the result of the excitable, wave-like dynamics of the actin cytoskeleton. New work shows that, in migrating cells, protrusion waves arise from mechanochemical crosstalk between adhesion sites, membrane tension and the actin protrusive machinery.

In order to migrate, eukaryotic cells have to transduce intracellular forces to the extracellular environment. A unifying theme is that the retrograde force produced by actin filaments growing against the leading plasma membrane is transduced to the substrate, e.g. via transmembrane adhesion receptors [1]. While this principle is of broad relevance, the spatiotemporal regimes under which such mechanocoupling arises can be diverse. Most cells show some kind of oscillatory morphodynamic patterns, such as protrusion–retraction cycles or wave-like undulations of their surface curvature. These shape changes define the different strategies of how cells move and, for some amoeboid cell types, it has been suggested that coordinated deformations can even endow them with the capacity to swim within viscous media [2,3]. How such, often oscillating, dynamics arise is largely unknown, but it is firmly established that the actin cytoskeleton generates almost all intracellular forces. In this issue of *Current Biology*, Barnhart et al. [4] now demonstrate how an interplay between three feedback loops involving actin-driven protrusion, adhesion site formation and membrane tension can generate laterally propagating protrusion waves.

For their study, Barnhart *et al.* [4] have used the simplest known paradigm for actin-driven cell motility: the fish keratocyte. These cells, derived from fish scales, migrate spontaneously and steadily when plated on an adhesive surface. Keratocytes display a stereotypic flat, fan-like morphology, shape changes over time are minimal, and there is almost no relative slippage between the substrate and the actin network growing from the leading edge. The leading edges of these cells represent expanding actin networks surrounded by the bag of plasma membrane and thus reduce the three-dimensional and temporally complex phenomenon of cell motility to a two-dimensional, largely homeostatic problem. In other words: as long as there is no thorough understanding of keratocyte motility, there is no understanding of cell migration.

In previous work, these authors found that, when plated on highly adhesive surfaces, keratocytes often show a remarkable behavior that is rare under intermediate adhesion conditions: they switch from the steady shape to oscillatory waving, where a new lamellipodium is initiated at the front and then travels laterally until it vanishes at the side of the cell [5]. Occasionally, two waves are initiated at the front of one cell, leading to a breaststroke pattern, whereby one wave travels to the left and the other to the right. The authors took a very quantitative morphometric approach and found that the adhesiveness of the substrate not only increases the frequency of traveling wave formation but at the same time decreases the width and the lifetime of the lamellipodium. This behavioral switch was induced not only by changing substrate adhesiveness but also by modifying the stability of adhesion sites, with pharmacological stabilization or de-stabilization of adhesion sites leading to more or less waving, respectively.

Temporal oscillations of lamellipodia are seen in most cell types, and fibroblasts and epithelial cells show regular protrusion–retraction cycles [6]. It has been suggested that such cycles are coupled to retrograde transport of molecular regulators that occurs together with the actin flow. In their new study, Barnhart *et al.* [4] considered this option, but when they measured retrograde actin transport in waving lamellipodia they found that there was no slippage between actin and substrate. This allowed them to conclude that actin polymerization itself rather than coupling to the substrate defines the propagation of the protrusive wave and that a wave ultimately dies when polymerization stalls. The spatial coupling between the travelling wave front and the adjacent sections of the

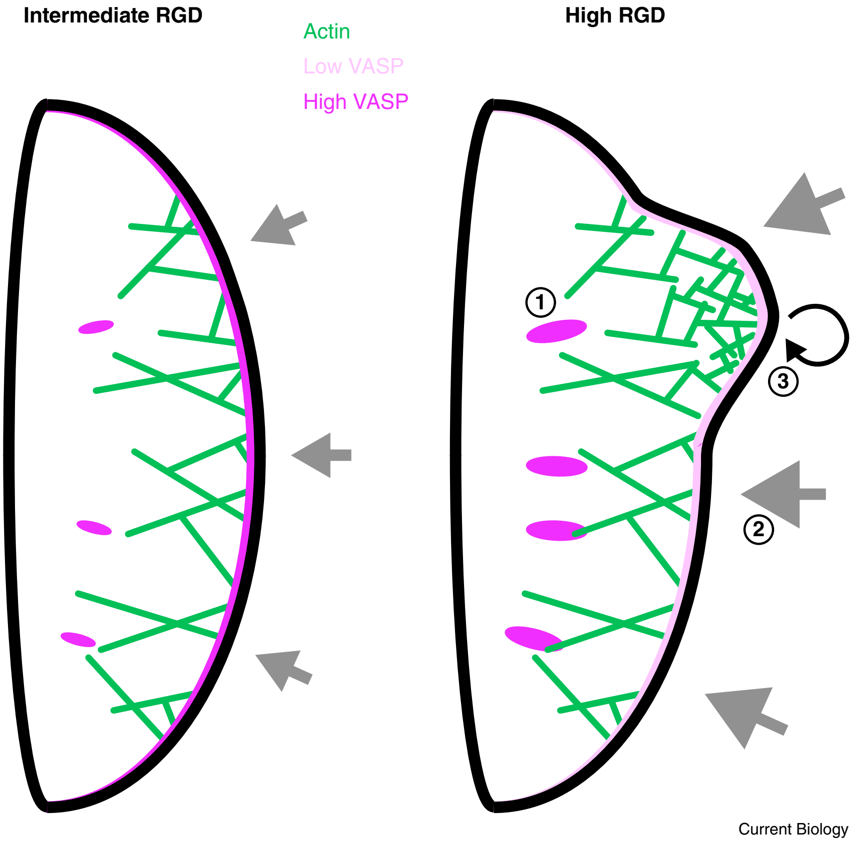

Figure 1. A model describing the interplay between adhesion, protrusion and membrane tension.
Keratocytes plated on substrates of intermediate adhesiveness show continuous protrusion of the leading edge. On highly adhesive substrates, the cells switch to an oscillatory 'waving' behavior. Three feedback loops govern wave formation in keratocytes migrating on high concentrations of RGD peptide, i.e. under high adhesion conditions: (1) large adhesions forming on high RGD accumulate large amounts of VASP, which is therefore depleted from the leading edge; (2) global inhibition of protrusion by increased membrane tension (denoted by large grey arrows); and (3) local positive feedback of increased protrusion on branching at the site of wave formation drives the propagation of the wave across the leading edge.

leading edge could be mediated either by the diffusion of an actin regulatory molecule or by the growth of the branched actin network itself. Given that the lateral propagation rate of the wave was strictly proportional to the maximal rate of protrusion velocity, a diffusive regulator — which should instead drive lateral propagation proportionally to the square root of its own diffusion constant — seemed unlikely.

The key question arising was how do adhesion sites talk to the leading edge? From the various actin regulatory factors that associate with both adhesions and the leading front, the authors focused on VASP, a factor with a dual function as an anti-capping protein and an elongating factor. The leading edge association of VASP was previously shown to faithfully correlate with protrusion speed in many different cell types [7]. Indeed, overexpression of VASP in keratocytes reduced the fraction of waving cells, essentially shifting the high adhesion phenotype toward the lower adhesion phenotype. These data suggested that adjacent adhesion sites titrate VASP from the leading edge and thereby keep the protrusion from growing under high adhesion conditions.

These findings drew a sufficiently simple picture to develop a mathematical model of the waving protrusion. Here, a protrusion is initiated when the local density of actin barbed ends exceeds a critical threshold to overcome lateral membrane tension (which equilibrates over the whole cell). VASP either increases barbed end density (by antagonizing capping) at the leading edge or is sequestered to adhesion sites. Barnhart *et al.* [4] found that three feedback loops between actin polymerization, membrane tension and adhesion site formation were sufficient to recapitulate the experimental data. The model also predicted that VASP should accumulate at the leading edge prior to wave initiation, which was confirmed experimentally.

So, in this new work, Barnhart *et al.* [4] demonstrate how a travelling wave can arise from a very simple set of mechanochemical feedbacks (Figure 1) and suggest that such waves may constitute a general module that could drive excitable actin dynamics in other contexts, like cell division, chemotaxis and neuronal communication. When cells migrate in three dimensions they deform with complex dynamic patterns and these dynamics have to be coordinated with geometric and adhesive features of the environment. It will probably take a long time for us to understand how the cell orchestrates its cytoskeletal machinery: the new study stresses the importance of reductionist but still adequate model systems to mechanistically understand dynamic phenomena.

REFERENCES

1. Case, L.B., and Waterman, C.M. (2015). Integration of actin dynamics and cell adhesion by a three-dimensional, mechanosensitive molecular clutch. Nat. Cell Biol. *17*, 955–963.
2. Barry, N.P., and Bretscher, M.S. (2010). Dictyostelium amoebae and neutrophils can swim. Proc. Natl. Acad. Sci. USA *107*, 11376–11380.
3. Driscoll, M.K., McCann, C., Kopace, R., Homan, T., Fourkas, J.T., Parent, C., and Losert, W. (2012). Cell shape dynamics: from waves to migration. PLoS Comput. Biol. *8*, e1002392.
4. Barnhart, E.L., Allard, J., Lou, S.S., Theriot, J.A., and Mogilner, A. (2017). Adhesion-dependent wave generation in crawling cells. Curr. Biol. *27*, 27–38.
5. Barnhart, E.L., Lee, K.C., Keren, K., Mogilner, A., and Theriot, J.A. (2011). An adhesion-dependent switch between mechanisms that determine motile cell shape. PLoS Biol. *9*, e1001059.
6. Lee, K., Elliott, H.L., Oak, Y., Zee, C.T., Groisman, A., Tytell, J.D., and Danuser, G. (2015). Functional hierarchy of redundant actin assembly factors revealed by fine-grained registration of intrinsic image fluctuations. Cell Syst. *1*, 37–50.
7. Rottner, K., Behrendt, B., Small, J.V., and Wehland, J. (1999). VASP dynamics during lamellipodia protrusion. Nat. Cell Biol. *1*, 321–322.